Distinct chromatin regulators downmodulate meiotic axis protein deposition and DNA break induction at chromosome ends

Adhithi R. Raghavan[1], Kieron May[2], Vijayalakshmi V. Subramanian[1,3], Hannah G. Blitzblau[1], Neem J. Patel[1], Jonathan Houseley[2], Andreas Hochwagen[1*]

Affiliations:

1. Department of Biology, New York University, New York, NY 10003, USA
2. Epigenetics Programme, Babraham Institute, Cambridge, CB22 3AT, UK
3. Department of Biology, IISER Tirupati, Tirupati, 517507, Andhra Pradesh, India

*Corresponding Author (andi@nyu.edu)

Current Affiliations: N.J.P. - Basecamp Research, London, UK

Abstract:

In many organisms, meiotic crossover recombination is suppressed near the extreme ends of chromosomes. Here we show that multiple, often chromosome-specific, suppressive mechanisms with differing ranges combine to achieve the consistently low enrichment of recombination-promoting axis proteins and downregulation of DNA double-strand breaks (DSBs) within 20 kb of telomeres in *Saccharomyces cerevisiae*. Suppression of axis proteins is associated with *cis*-encoded signals, including reduced coding density and the subtelomeric Y' elements, which are present at many chromosome ends, but also requires chromatin modifiers, including the histone methyltransferase Dot1 and the Sir silencing complex. We show that Dot1 suppresses Sir complex activity at least in part independently of its canonical target, H3K79, to downmodulate axis protein deposition near chromosome ends. In parallel, the Sir complex, but not Dot1, suppresses the induction of DSBs by limiting the openness of promoters, the preferred sites of meiotic DSB formation. The separable downmodulation of axis protein deposition and DSB induction likely contributes to the robust reduction of meiotic recombination effectors near chromosome ends.

Keywords: meiotic DSBs, subtelomeres, axis proteins, chromatin modifiers, Dot1, Sir2, Sir3

Introduction:

Meiosis is a specialized type of cell division that generates haploid gametes from diploid progenitor cells and plays an essential role in promoting genetic diversity [1]. Meiosis begins with a single round of DNA replication followed by two rounds of chromosome segregation, first segregating homologous chromosomes and then sister chromatids [2,3]. Accurate segregation during meiosis I relies on meiotic crossover recombination, which exchanges DNA between homologous chromosome pairs and, together with sister chromatid cohesion, forms a physical connection between them [4]. Meiotic recombination is initiated by programmed DNA double-strand breaks (DSBs), which are catalyzed by Spo11, a highly conserved topoisomerase-like enzyme [5].

Although DSBs can occur throughout the genome, their frequencies vary widely. Chromosomal regions classified as “hot” experience frequent DSBs, whereas “cold” regions, including centromeres and chromosome ends, rarely undergo breakage [6]. Hotness results from a complex interplay of factors, including local base composition, chromatin modifications, meiotic chromosome architecture, as well as environmental factors [5,7-9].

In addition to DSBs, the differential distribution of meiosis-specific axis proteins, which localize at the base of the loop-axis structure of meiotic chromosomes, has a major impact on recombination levels across the genome. Axis proteins can promote DSB activity and are also essential for directing repair toward the homologous chromosome, and thus crossover formation [6,10-12]. In *S. cerevisiae*, elevated binding of the axis proteins Red1 and Hop1 is often associated with markers of crossover repair [13,14]. Red1 and Hop1 are recruited to the base of chromatin loops by the meiotic Rec8-cohesin complex but can also bind directly to chromatin through the nucleosome-binding activity of Hop1 [13,15,16], leading to two independent modes of axis protein-dependent patterning of meiotic recombination.

In *S. cerevisiae*, levels of DSBs and crossover formation exhibit a distinctive pattern near chromosome ends. Levels are elevated above genome average in the end-adjacent regions (EARs), large chromosomal regions located 20-120 kb from chromosome ends but notably reduced within ~20 kb from telomeres [11,17-20]. This depletion in the last ~20 kb is likely important for two reasons. First, these regions are enriched for repetitive DNA sequences that are vulnerable to non-allelic homologous recombination (NAHR) and genome rearrangements [21]. Second, crossovers near chromosome ends are less effective at forming stable connections between homologous chromosomes and may lead to chromosome mis-segregation if they are the only connection between homolog pairs [22]. Indeed, recombination events near telomeres are linked to a higher risk of Trisomy 21 (Down syndrome) in humans [23,24].

S. cerevisiae chromosome ends consist of several distinct genomic domains (**Fig. 1a**) [25,26]. In addition to telomerase-templated telomeric repeats that cap chromosome ends, "telomere-associated sequences" contain repetitive Y' and X elements. In addition, the "subtelomeric domains" extend inward for an average of about 20 kb from telomeres. Subtelomeric domains are relatively gene-poor regions enriched in gene families [27,28]. In vegetative cells, the telomeric repeats and X elements recruit the Sir2/Sir3/Sir4 histone deacetylase complex, establishing transcriptional silencing. This silent chromatin can spread over limited distances into the subtelomeric domains [29]. The subtelomeric domains, in turn, are defined by a unique chromatin signature, which includes a relative depletion of active chromatin marks [28,30]. Whether similar chromatin patterns exist during meiotic recombination is unknown.

Previous studies of meiotic recombination in *S. cerevisiae* have consistently shown a depletion of DSBs in X and Y' elements as well as in the subtelomeric domains [11,17,31,32]. While the mechanisms governing DSB suppression in X and Y' elements remain largely unexplored, the reduced DSB levels in the subtelomeric domains are accompanied by lower recruitment of DSB-promoting factors, such as Rec114 [33], and diminished abundance of Hop1 [19]. Hop1, which

recruits Rec114 [12], is currently the most upstream regulator of recombination known to be depleted about 20 kb from chromosome ends. However, the specific mechanisms controlling this altered distribution of Hop1 - and whether its depletion is linked to the suppression of meiotic DSBs - is not understood.

Results:

Distinct axis protein enrichment patterns at chromosome ends

Given the reduced axis protein enrichment near chromosome ends and their critical role in meiotic DSB formation and repair, we investigated how axis proteins interact with telomere-associated sequences and subtelomeric domains. These regions are often excluded from sequence-based analyses because of variations in telomere organization even among closely related yeast strains [25,34,35], and because the abundance of repetitive sequences and gene families creates challenges for uniquely assigning sequencing reads. Therefore, we tailored our analysis pipeline to account for these unique biological features. To reduce structural mapping artifacts, we mapped reads to high-quality end-to-end chromosome scaffolds of our experimental strain (SK1) [35], rather than the commonly used S288c reference. Although the inherent instability of subtelomeric domains means that individual SK1 isolates may differ from the SK1 reference at some ends, this approach eliminates the profound telomere-proximal sequence differences between SK1 and S288c as a major source of error. Further, by exclusively considering optimal matches, we maximized the number of confidently mapped reads, leveraging inherent sequence polymorphisms within telomeric repeat sequences for unique mapping.

To validate our pipeline, we assessed mapping and coverage characteristics in unenriched input datasets. Even in the highly repetitive X and Y' elements, our pipeline was able to uniquely map 12.8% and 0.87% of single-end reads and 15.2% and 12.8% of paired-end reads, respectively.

In subtelomeric domains as a whole (within 20 kb from chromosome ends), unique mapping rates were higher, averaging 24.1% for single-end reads and 32.2% for paired-end reads (**Supplementary Fig. 1a**). In addition, we observed no systematic differences in fragmentation efficiency (**Supplementary Fig. 1b**) and only minor differences in sequence coverage due to incomplete X-element annotation (**Supplementary Fig. 1c**), indicating that telomere-proximal regions are sampled comparably to the chromosome interior.

If a read had multiple equally well-mapped results, our pipeline randomly selected one location as the primary alignment for the read. This approach did not affect metagene analyses but significantly improved signal clarity at individual chromosome ends by closing coverage gaps caused by a lack of polymorphisms. Comparative analysis of ChIP profiles with and without multiple-mapping reads revealed no qualitative differences (**Supplementary Fig. 1d**).

With this strategy, we analyzed the distribution of axis proteins at chromosome ends using previously published ChIP-seq datasets [16,19,36]. Meta-analysis showed that Red1 and Hop1 were depleted below genome average within 20 kb of chromosome ends and enriched above genome average in the EARs (20-120 kb; **Fig. 1b-c**), consistent with previous studies [19]. Axis protein depletion in the first 20 kb was observed across all chromosome ends and thus could not be attributed to individual telomere outliers (**Supplementary Fig. 2, 3a**).

Yeast chromosome ends are characterized by telomeric repeats, $(TG_{1–3})_n$, and telomere-associated sequences, which include the Y' and X elements [37]. The long Y' elements (4-7 kb) are not found on all ends and can occur as one or multiple copies, whereas a short X element (~500 bp) is detectable at nearly all chromosome ends [35,38] (**Fig. 1a, Supplementary Fig. 2**). Based on these features, we classified chromosome ends into two categories: X-only ends, which contain only the X element, and XY' ends, which include both X and Y' elements. Because X elements are relatively small and therefore more difficult to annotate, we classified

ends containing a Y′ element as XY′, whereas ends lacking a Y′ element were categorized as X-only. The two ends without annotated X or Y′ elements were also included in the X-only category. Meta-plots of Red1 and Hop1 profiles revealed that axis protein enrichment differed between these two categories. X elements at X-only ends exhibited axis protein enrichment close to the genome average, indicating that isolated X elements have a substantial propensity for axis protein recruitment (**Fig. 1d**). By contrast, X elements at XY' ends showed Red1 and Hop1 enrichment below the genome average (**Fig. 1d-e**). Meta-analyses revealed an axis protein binding site at the telomere-proximal side of the Y' element that may act as a local sink for axis protein recruitment (**Fig. 1f**).

The variable presence of Y' elements also raised the question of whether axis protein depletion is more appropriately assessed by aligning chromosome ends at the X elements. However, metagene analysis anchored on the X elements instead of the telomeres showed a substantially weakened depletion signal in meta-analyses (**Supplementary Fig. 4a**). Although this weakened signal is likely partly due to increased noise from incomplete X-element annotation, the noticeably more uniform depletion when anchoring on telomeres indicates that the biologically relevant anchor for the observed suppression of axis protein deposition is the chromosome end.

Multiple *cis*-encoded features correlate with axis protein depletion near telomeres

Further analysis revealed that although both XY' and X-only chromosome ends have reduced axis protein binding compared to the genome average, the depletion is stronger at XY' ends (**Fig. 2a, Supplementary Fig. 4b**). The biased depletion at XY' ends was also apparent when the Y' elements were masked out from the analysis, demonstrating that the depletion is not solely due to differential axis protein enrichment on Y' elements (**Supplementary Fig. 4c**). It is possible that Y' elements influence axis protein deposition. Alternatively, XY' ends may be distinguished by other sequence features that lead to lower accumulation of axis proteins.

Notably, as axis protein levels are also lower than genome average at X-only ends, there must be at least two mechanisms suppressing axis protein recruitment near telomeres.

To determine whether the suppression of axis protein binding is due to telomere proximity or intrinsic sequence features, we analyzed chromosome fusions, in which subtelomeric domains were relocated to the chromosome interior [39]. These chromosomes showed overall normal Red1 enrichment, except for regional changes around centromeres, as noted previously [39]. At fused chromosome ends, axis protein distribution mirrored that of native, unfused ends in two different sequence background (S288c and SK1; **Fig. 2b-c**), suggesting that reduced axis protein enrichment at chromosome ends is driven by specific sequences encoded at chromosome ends rather than by telomere proximity.

In two cases, the fusion process also eliminated Y' elements without apparent effects on axis protein enrichment (**Fig. 2b**). Thus, at least at these two ends, Y' elements do not have detectable long-range effects on axis protein enrichment. However, because the engineering of chromosome fusions required unique sequences for targeting the translocation events, the fusion points are in both cases >18kb from the nearest Y' element. Thus, we cannot exclude the possibility that Y' elements affect axis protein enrichment over shorter chromosomal distances.

Across the genome, gene-rich regions exhibit overall higher axis protein enrichment [13,16]. As the subtelomeric domains are comparatively gene-poor [27,28], we wondered how well local coding density (the fraction of DNA that encodes open reading frames) correlated with axis protein enrichment. This analysis revealed a strong correlation between the regions of reduced coding density and axis protein depletion (**Fig. 2c-d**). In addition, binning the genome into 20-kb bins showed a positive correlation between coding density and average Red1 binding, similar to the effect seen across the genome (**Fig. 2e**). Thus, reduced coding density may partially underlie the reduced axis protein recruitment within 20 kb of telomeres. Interestingly, this correlation was

absent in the EARs (**Fig. 2e**), presumably reflecting the specialized regulation of axis protein deposition in these regions [19].

Rec8-dependent and independent pathways mediate axis protein localization at chromosome ends

Chromosomal recruitment of Red1 and Hop1 is mediated by two parallel pathways. The meiotic Rec8-cohesin complex preferentially recruits axis proteins to sites of convergent transcription [16], whereas the chromatin-binding region (CBR) of Hop1 directs axis proteins to nucleosome-dense regions ("islands") characterized by higher coding density [13,16]. We sought to determine whether the depletion of axis proteins near chromosome ends could be attributed to reduced activity of one of these pathways.

Intriguingly, Rec8-cohesin levels in the subtelomeric regions were comparable to the genome average. Although enrichment trended slightly lower, the depletion was within the 95% confidence interval of a bootstrapped distribution (p=0.37) and thus was not significantly different from the rest of the genome (**Fig. 1b-c**). Therefore, the depletion of Hop1 and Red1 in the subtelomeric domains is not simply due to reduced Rec8-cohesin binding in these regions.

The regions enriched for Red1 and Hop1 in the telomere-associated sequences were also enriched for Rec8: Rec8 was bound more strongly to the X elements of X-only ends than to XY' ends (**Fig. 1d-e**) and formed a strong peak at the telomere-proximal side of Y' elements (**Fig. 1f**). This peak coincided with the 3' end of the Y'-encoded open reading frame (ORF), consistent with other chromosomal Rec8 peaks, which are typically enriched downstream of ORFs [16,40]. Previous studies have demonstrated that active transcription can induce the sliding of the cohesin ring and direct axis protein association to the end of ORFs [16,41,42]. Therefore, transcription of the Y' ORF may similarly influence axis protein deposition within Y' elements.

The coincident binding of axis proteins and Rec8 supports the hypothesis that Rec8-cohesin is an important contributor to axis protein deposition at chromosome ends. To directly test this possibility, we examined Red1 binding in a *rec8* mutant strain using spike-in normalized ChIP-seq datasets [13,36]. In the subtelomeric domains, Red1 levels were significantly reduced in the *rec8* mutant compared to wild type (**Fig. 3a-b**). Importantly, the remaining Red1 enrichment was no longer depleted in the subtelomeric domains. These data suggest that the molecular mechanism that reduces axis proteins in the subtelomeric domains interferes with the Rec8-dependent recruitment of axis proteins.

On the other hand, analysis of a *hop1-phd* mutant, which lacks the CBR [13,15], revealed only minor effects in the subtelomeric domains (**Fig. 3a-b**). However, we consistently noted reduced Red1 binding in the neighboring EARs (**Fig. 3a**), implying a role for the Hop1 CBR in promoting axis protein enrichment in the EARs. In line with the two recruitment mechanisms acting in parallel [13,15], the persistent subtelomeric axis protein signal in *rec8* mutants was abolished upon introduction of the *hop1-phd* mutation (**Fig. 3a-b**). Similar additive effects were observed in the X and Y' sequences (**Fig. 3c-d**). These data indicate that both pathways of axis recruitment contribute additively to Red1 binding at chromosome ends. However, the Rec8-dependent pathway, which is responsible for recruiting the majority of Red1, is the regulatory target for the relative depletion of axis proteins from chromosome ends.

Dot1 is required for subtelomeric depletion of axis proteins

Subtelomeric regions share qualitative similarities with pericentromeric regions, particularly in the differential enrichment of axis proteins and Rec8-cohesin. Both regions show a relatively higher abundance of Rec8-cohesin compared to Red1, with most data points falling below the genome-wide regression line (**Fig. 4a**)**.** At pericentromeres, this differential enrichment of axis factors persists even if the centromere itself is inactivated [39], indicating that the local DNA

sequence or chromatin environment influences axis protein binding. Given the distinct chromatin state of subtelomeric domains, we investigated whether chromatin modifiers specific to these regions contribute to axis protein depletion.

We focused our analysis on histone marks related to meiotic DSB formation or those specifically different in the subtelomeric domains [30,43-46]. ChIP-seq analysis identified two marks - H3K4me3 and H3K79me3 - that closely matched the pattern of axis protein depletion (**Fig. 4b**, **Supplementary Fig. 5a**). Both marks are long-lasting indicators of active gene expression that are depleted from subtelomeric domains [28,30] and have been implicated in the control of meiotic DSB formation [43,46]. To explore the role of these histone modifications in axis protein depletion, we used spike-in normalized ChIP-seq [36] to analyze Red1 in mutants lacking Set1 or Dot1, the enzymes responsible for the trimethylation of H3K4 and H3K79, respectively. In *set1Δ* mutants, subtelomeric Red1 binding patterns were indistinguishable from wild-type, although we observed an overall reduction in Red1 binding (**Fig. 4c-e, Supplementary Fig. 5b-c**), consistent with previous analyses [36]. In contrast, *dot1Δ* mutants exhibited a marked redistribution of Red1. Red1 levels were relatively elevated in the Y' and X elements and no longer significantly different from genome average in the subtelomeric domains (p=0.16) but were reduced in the EARs (**Fig. 4c-e, Supplementary Fig. 5b-c**), indicating that Dot1 is an important regulator of axis protein distribution. In addition, Red1 levels in *dot1Δ* mutants also trended lower in the pericentromeric regions (p=0.06 after Benjamini Hochberg correction; **Supplementary Fig. 5d-e**). This effect is opposite to the increase seen in the subtelomeric domains and indicates that subtelomeric domains and pericentromeres use different mechanisms to achieve a relative depletion of Red1 compared to Rec8-cohesin.

To test whether the effects of Dot1 on Red1 recruitment are related to H3K79 trimethylation, we analyzed mutants, in which H3 lysine 79 was changed to arginine (*hht1/2-K79R*). These mutants recapitulated the drop in Red1 levels in the EARs (**Fig. 5a**), indicating that Dot1

promotes axis protein binding in the EARs by methylating H3K79. However, Red1 levels in *hht1/2-K79R* mutants also decreased in the subtelomeric domains and in the Y' and X elements (**Fig 5a-d**) and did not decrease in the pericentromeric regions (**Supplementary Fig 5d-e**). These observations suggest that a H3K79-independent activity of Dot1 mutates the reduction of axis proteins near chromosome ends and centromeres. MNase-seq analysis of *dot1Δ* mutants failed to reveal obvious changes in chromatin accessibility in the subtelomeric domains or the pericentromeres **(Supplementary Fig. 5f-g)**, suggesting that the effects on Red1 recruitment seen in *dot1* mutants are not the result of altered nucleosome occupancy.

As Dot1 primarily methylates H3K79 across gene bodies, we separated Red1 signals into genic and intergenic regions. Intriguingly, the reduced binding of Red1 in the chromosome interior in *dot1Δ* mutants primarily affected intergenic regions whereas the increase in Red1 association near chromosome ends in *dot1Δ* mutants occurred predominantly on gene bodies (**Fig. 4f**). These data indicate that the chromatin requirements for axis protein recruitment differ between chromosome ends and the chromosome interior and that Dot1 plays multiple roles in controlling axis protein recruitment, only some of which require H3K79 methylation.

Effects of Dot1 on axis protein deposition depend on Sir3

One consequence of *DOT1* disruption is the spreading of the Sir complex beyond its usual boundaries [47,48]. To test whether the Sir complex is involved in the axis protein recruitment defect of *dot1* mutants, we determined the distribution of Red1 in *sir3* mutants using spike-in normalized ChIP-seq analysis. Binding levels of Red1 in the EARs were higher in the *sir3* mutants (**Fig. 6a**), consistent with previous analyses of Hop1 in *sir2* mutants [19], but meta-analysis revealed no significant difference in the average depletion of Red1 in the last 20 kb between *sir3* and wild-type strains (**Fig. 6a-b**). Similarly, meta-plots of average Red1 profiles on X and Y' elements in *sir3* mutants showed no new peaks compared to wild-type (**Fig. 6c-d**),

although enrichment levels were lower on both types of X element (**Fig. 6c**). Thus, the Sir complex is not a major regulator of telomere-proximal axis protein depletion in wild-type cells.

Intriguingly, however, mutation of *sir3* reversed many of the Red1 recruitment phenotypes of *dot1* mutants, including the increased Red1 binding in the subtelomeric domains and the decreased binding in the EARs and pericentromeres (**Fig. 6a-b, Supplementary Fig. 6a-b**). Moreover, the binding pattern of Red1 across X and Y' elements in the *sir3 dot1* double mutant matched the phenotype of the *sir3* mutant rather than the *dot1* mutant (**Fig. 6a-b**). This phenotypic epistasis indicates that Dot1 counteracts the activity of the Sir complex to control Red1 distribution.

Conservation of Sir-dependent telomeric heterochromatin during meiotic recombination

To better understand the role of the Sir complex in meiosis, we analyzed the genomic distribution of Sir3 in wild-type cells by ChIP-seq. In vegetative cells, the Sir complex establishes silent chromatin domains at mating-type loci and telomere-associated sequences [49,50]. At some chromosome ends, Sir chromatin also spreads from the X element into the neighboring subtelomeric domains [29,51], although spreading across entire subtelomeric domains is only observed under conditions of Sir overexpression [30].

Our observations at the time of meiotic induction and during the peak of DSB formation (3 hours post-induction) revealed consistent Sir3 binding patterns (**Fig. 7a, Supplementary Fig. 7**). Sir3 was enriched at both types of X elements, although binding on X elements at XY' ends was lower than that observed at X-only ends (**Fig. 7a-b**). Sir3 was also enriched upstream of the 5' end of the Y'-encoded ORF (**Fig. 7c**). In addition, we observed heterogeneous spreading of Sir3 from subtelomeric X elements into adjacent domains on certain chromosome ends. For example, on chrVII-L, Sir3 spread approximately 6 kb from the X element during early prophase I (3 hours post-induction), whereas no detectable spreading occurred on chrVI-L (**Fig. 7d-e**).

Spreading distances varied across chromosome ends (**Supplementary Fig. 8a-b**) and did not correlate with the presence of Y' elements (**Supplementary Fig. 7**), mirroring the distribution of Sir proteins in vegetative cells [29,30]. These findings indicate that Sir-dependent telomeric heterochromatin remains largely unchanged as cells initiate meiotic recombination.

To determine whether subtelomeric domains with Sir3 spreading exhibit altered transcription of underlying genes, we conducted mRNA-seq analysis on samples collected 3 hours post-meiotic induction in the presence or absence of *SIR3*. Plotting relative fold changes in mRNA levels as a function of the average Sir3 occupancy in the 250 bp upstream of each ORF revealed a significant correlation between Sir3 occupancy and increased mRNA levels upon *SIR3* deletion (**Fig. 7f**). Given the prominent Sir3 peak observed at the start of the Y' element metaplot (**Fig. 7c**), we also analyzed Y' element expression at 3 hours post-meiotic induction. The average Y' element expression was significantly increased in the absence of *SIR3* (**Supplementary Fig. 8c**). These results indicate that the transcriptional effects of Sir3 are linked to sequences where Sir3 binds, as detected by ChIP-seq.

Sir-dependent transcriptional silencing in vegetative cells is thought to occur by chromatin compaction and promoter occlusion [52]. MNase-seq analysis of wild type and *sir3* mutants 3h after meiotic induction, revealed a strong Sir3-dependent drop in the relative number of sequenced MNase cleavage fragments in the subtelomeric domains, consistent with chromatin compaction (**Fig. 7g**). Interestingly, the effects on chromatin compaction as measured by MNase-seq extended across more than 20 kb, contrasting with much more limited extent of detectable Sir3 spreading (**Supplementary Fig. 8a**). These data indicate that Sir3 can influence chromatin compaction even in regions where it is not measurably enriched, possibly through the role of the Sir complex in anchoring telomeres in the nuclear envelope [53].

Sir proteins protect X elements and regions of Sir spreading from meiotic DSBs

We wondered how Sir-dependent heterochromatin and Dot1-dependent axis protein suppression interface with the meiotic DSB machinery near chromosome ends. Genome-wide DSB levels had previously been determined by microarray analysis in *sir2Δ rad50S* strains, but the repetitive nature of the subtelomeric domains had limited coverage, and the X and Y' elements were not included [54]. More recently, DSB formation in *sir2Δ* strains was also analyzed using Spo11-oligo sequencing [19], which sequences the DNA fragments that remain covalently attached to Spo11 after cleavage [11], although telomere-proximal DSB formation was not investigated in that study. Analysis of the Spo11-oligo dataset revealed a significant increase in DSB levels on X elements but not Y' elements in *sir2Δ* strains (**Fig. 8a**). This pattern mirrors the relative enrichment of Sir3 in these elements, indicating that Sir chromatin suppresses DSB formation in the X elements.

We also observed increased DSB formation in the subtelomeric domains in *sir2Δ* mutants. Increased DSB induction was correlated with the extent of Sir3 occupancy in wild-type cells (**Supplementary Fig. 9a**). Accordingly, increased DSB formation was also correlated with elevated gene expression in the same regions in *sir3* mutants but not in the rest of the genome (**Supplementary Fig. 9b**). These findings suggest that elevated promoter openness, which enables increased gene expression, also creates a window for meiotic DSB formation.

To complement and expand this analysis, we analyzed *sir3, dot1Δ*, and *sir3 dot1Δ* mutants by TrAEL-seq, which sequences the exposed 3' ends that result from Spo11 cleavage [55]. To avoid signal changes due to DSB repair, this analysis was conducted in a repair-defective *dmc1Δ* background [56]. We observed several distinct effects on DSB formation near chromosome ends. In strains lacking *SIR3*, average hotspot intensity was significantly increased within 5 kb of X elements and the number of significant DSB hotspots nearly doubled in the same regions (**Fig. 8b-c**), consistent with the Spo11–oligo measurements in *sir2Δ* mutants. Notably, increased DSB formation occurred specifically at sites of increased MNase accessibility (**Fig. 8d**), strongly

supporting the model that Sir-dependent DNA occlusion suppresses DSB formation in the heterochromatic parts of the subtelomeric domains. On the other hand, deletion of *DOT1* did not measurably alter DSB formation in the 20 kb from chromosome ends (**Fig. 8b-d**), showing that the increased axis protein deposition in these regions does not translate into higher DSB activity. We also note that overall hotspot activity in the subtelomeric domains remained substantially below genome average in all mutants (**Fig. 8d-e**), indicating that additional layers of regulation contribute to DSB suppression at chromosome ends.

Intriguingly, TrAEL-seq analysis indicated differing genetic interactions between *DOT1* and *SIR3* in other parts of the genome. The most notable large-scale effect was a decrease in DSB levels in the *sir3 dot1Δ* double mutants 30-100 kb from chromosome ends, a genomic range that largely overlaps with the EARs (**Fig 8e**). The reason for this decrease is unclear but may reflect premature downregulation of DSBs in the EARs, which normally experience a longer window of DSB formation [19]. Further highlighting the different genetic interactions between *DOT1* and *SIR3*, DSB formation around centromeres was decreased to a similar extent in *dot1Δ* and *sir3* single mutants (**Supplementary Fig. 10a**), whereas DSB levels were increased around the ribosomal DNA locus in a Sir3-dependent manner in *dot1Δ* mutants (**Supplementary Fig. 10b**), consistent with previously observed Sir-dependent DSB induction in this region [57]. As discussed further below, the different interactions suggest a combinatorial code that allows these two chromatin regulators to adjust meiotic recombination in a region-specific manner.

Discussion:

Here, we show that key effectors of meiotic recombination, namely axis proteins and the DSB machinery, are suppressed by multiple layers of regulation at chromosome ends. Suppression involves regulation encoded in *cis* as well as protein-dependent activities, and we identified two

chromatin regulators, Dot1 and the Sir complex, which locally suppress axis protein deposition and DSB formation, respectively.

Our data suggest that at least two *cis*-encoded effects drive down axis protein binding near chromosome ends. First, ends encoding Y' elements show markedly lower levels of axis protein enrichment although it remains unclear whether the Y' elements themselves are involved in this effect as there is a prominent axis protein binding site next to the Y' ORF and there was no long-range impact of axis protein enrichment when Y' elements were deleted in chromosome fusions. In addition, we observed *cis*-encoded axis protein suppression that was uncorrelated with Y' elements. This signal could be related to the reduced coding density of the subtelomeric domains, which tracks remarkably well with the depletion of axis proteins, but could also be linked to other *cis*-regulatory aspects such as differential replication timing [33,58].

In addition, Dot1 negatively regulates axis protein deposition in X and Y' elements and the subtelomeric domains. This activity does not require H3K79 trimethylation and thus either depends on other methylation targets or on Dot1's methyltransferase-independent activities, several of which have been described [59,60]. Dot1 presumably interferes with Rec8-dependent axis protein recruitment as our analyses suggest that this pathway is specifically weakened near chromosome ends. Intriguingly, the increased axis protein deposition in *dot1* mutants is rescued by deletion of *SIR3*, suggesting that Dot1 counteracts the activity of Sir3 to regulate telomere-proximal axis protein deposition. An interplay between the Sir complex and Dot1 was previously shown to affect checkpoint regulation during meiotic recombination [61]. In vegetative cells, Dot1 helps constrain Sir-protein dependent silencing both through H3K79 trimethylation and by competing for the same nucleosomal binding site [62]. This two-pronged mechanism may explain why mutation of H3K79 was not sufficient to recapitulate the increased axis protein deposition seen in *dot1* mutants. Interestingly, even though the axis proteins act as recruitment platforms for the DSB machinery [12], increased axis protein deposition was not sufficient to increase DSB

formation in the telomere-proximal sequences in *dot1* mutants, indicating that additional layers of regulation suppress DSB formation in these regions.

We show that the Sir complex suppresses DSB formation near telomeres through local chromatin compaction of gene promoters, the preferred DNA substrates for DSB formation in yeast [11]. Our data strongly imply that DSB suppression is a direct consequence of the enrichment of Sir3 in these regions. Furthermore, the strict spatial overlap between increased MNase sensitivity and sites of DSB formation in *sir3* mutants provides one of the first pieces of direct evidence that nucleosomes block meiotic DSB formation *in vivo*. Nucleosome occupancy and meiotic DSB formation are strongly anticorrelated in *Saccharomyces* species and *Arabidopsis* [11,63,64], indicating that this fundamental mode of DSB patterning is conserved.

While this study focused on the subtelomeric regions, our genome-wide data also showed effects of Dot1 and the Sir complex in other parts of the genome, including the EARs, the pericentromeres, and the rDNA-flanking regions. H3K79me3 is abundantly present in those regions, and Dot1's distribution in vegetative cells closely matches H3K79me3 [65], suggesting that Dot1 and H3K79me3 may directly influence axis protein deposition and/or DSB formation in those regions. By contrast, Sir3 is not noticeably enriched in the EARs or the pericentomeres in our analyses. However, genome-wide effects of *sir* mutation on meiotic DSB formation were also noted previously [54]. It is possible that the Sir complex levels in these regions are too low to measure confidently. Alternatively, some effects may be indirect as both, the Sir complex and Dot1, are transcriptional regulators and thus could change the expression levels of key meiotic regulators to modulate regional axis protein deposition or DSB activity. Such indirect effects may also contribute to varying genetic interactions between the Sir complex and Dot1 observed in different genomic regions.

Chromosome ends differ in their sequence composition, presence of Y' elements, spreading of the Sir complex, and the location of genes, DSB hotspots, and axis binding sites, creating inherently chromosome end-specific variability in the range and presence of individual suppressive effects. Nevertheless, the combined effect of these layers of regulation results in a remarkably uniform downregulation of axis protein deposition and DSB induction within about 20 kb from chromosome ends (**Supplementary Fig. 3a-b**). Thus, overall selective pressure likely exists to reduce axis protein binding and DSB induction at chromosome ends, and multiple molecular mechanisms have the potential to satisfy this goal.

One selective pressure near chromosome ends is the need to suppress meiotic crossovers. Telomere-proximal crossovers are less effective at maintaining linkages between homologous chromosomes [66] and are associated with increased risk of Down syndrome in humans [23,24]. Axis proteins, in particular, are a logical target for such suppression, as they not only recruit DSB factors but also help target DSB repair to homologous chromosomes by preventing sister chromatid recombination [67]. Favoring repair from sister chromatids may also reduce the risk of non-allelic recombination events. Chromosome ends are especially prone to non-allelic homologous recombination because of their repetitive sequences and the close physical proximity of telomeres along the nuclear envelope during meiotic prophase [21,68,69]. Having multiple regulatory layers independently suppress axis protein deposition and DSB formation may thus establish a robust protective mechanism to shield chromosome ends from non-allelic and unproductive recombination and ensure proper meiotic chromosome segregation.

Methods and Materials:

Yeast strains and growth conditions:

All the strains utilized in this study belonged to the SK1 background, except for the analysis using the published fusion chromosomes, which are SK1/S288C hybrids or spike-in analysis (see Methods: Spike-in Normalization). The genotypes are detailed in **Supplementary Table 1.** For experiments using vegetative cells, cultures were grown in YPD medium overnight at room temperature until saturation. On the following day, the cells were diluted to an OD_{600} of 0.2 and incubated at 30°C until they reached an OD_{600} of 1. At this stage, 50 ml of culture was collected for ChIP-seq.

To induce synchronous meiotic cultures, strains were grown for 24 hours in YPD medium at room temperature. Cells were enriched in the G1 phase by inoculating them at OD_{600} = 0.3 in pre-sporulation BYTA medium (1% yeast extract, 2% bactotryptone, 1% potassium acetate, 50 mM potassium phthalate) for 16.5 hours at 30°C. Cells were washed twice with sterile water and transferred into SPO medium at OD_{600} = 1.9 (SPO: 0.3% potassium acetate, 0.001% acetic acid). Cultures were incubated at 30°C on a shaker, and the time of inoculation into SPO was defined as T = 0 hours. At the specified timepoints, 25 ml of culture was collected for ChIP-seq and 1.6 ml for mRNA-seq. The synchrony of meiotic cultures was validated using flow cytometry.

Chromatin immunoprecipitation (ChIP) & Illumina sequencing:

Cells collected at the indicated timepoints (T = 3h unless noted otherwise) were pelleted and immediately crosslinked for 30 minutes in a 1% formaldehyde solution at room temperature with gentle shaking. Subsequently, the crosslinking reaction was quenched by incubating the cells for 5 minutes at room temperature in a 125 mM glycine solution. Following this, the cells were processed according to the protocol outlined in [16] and immunoprecipitated with 2.5 µl of either anti-Sir3 (HM01065, kind gift of S. Bell), anti-Red1 (#16440, kind gift of N. Hollingsworth) or anti-H3K79me3 (abcam, ab2621). For spike-in normalization (SNP-ChIP [36]), SK288c cross-linked

meiotic samples were added to respective samples at 20% prior to ChIP processing. Library preparation, quality, and quantity checks were then performed as described in [15]. All the prepared chromatin immunoprecipitation (ChIP & SNP-ChIP) libraries were sequenced as 150-bp paired-end reads on Illumina NextSeq 500 or Element Biosciences' Aviti instruments. The sequencing runs were conducted by the Genomics Core at New York University Center for Genomics and Systems Biology.

Processing ChIP-seq reads from Illumina sequencing:

Illumina sequencing reads were aligned to the SK1 genome [35] using Bowtie 2 (Version 2.4.2) [70]. To improve mapping of reads to repetitive subtelomeric regions, the Bowtie 2 read reporting mode was configured to allow multiple alignments, reporting the best match. MACS2 2.1.1 was used to extend reads in the 5'-> 3' direction to a final length of 200 nt. SPMR (signal per million reads) normalization was applied to both input and ChIP pileups using MACS2. The resulting fold-enrichment files were used for downstream analysis in R. The ChIP-seq pipeline and analysis scripts are available on the Hochwagen Lab GitHub page https://github.com/hochwagenlab/ChromosomeEnds.git.

mRNA-sequencing & analysis:

mRNA was extracted from cells collected at T=3h. mRNA extraction, first- and second-strand synthesis, and library preparation were conducted following the procedures outlined in [71]. The resulting libraries were subjected to sequencing as 150-bp paired-end reads on Illumina NextSeq 500 instruments. The sequencing run was executed by the Genomics Core at New York University Center for Genomics and Systems Biology. The GTF (General Transfer Format) file was modified to include all completely annotated Y' elements. Subsequently, reads obtained from Illumina sequencing were aligned to the SK1 genome [35], and the counts mapping to the modified SK1 gtf file were determined using the nf-core RNA-Seq pipeline [72]. The relative

abundances, measured as Transcripts per million (TPM) in the Salmon [73], were utilized for downstream analysis in R.

Spo11-oligos mapping:

Published Spo11-oligo dataset from WT and *sir2Δ* strains [19,74] were analyzed. Adaptors were removed from the reads using fastx_clipper fomr the FASTX Toolkit (version 0.0.14) and reads shorter than 15 nt were discarded. The clipped reads were aligned to the SK1 genome [35] using Bowtie 2 (Version 2.4.2) [70]. The read alignment mode was set to local, and the reporting mode allowed multiple read alignments while reporting the best alignment. SPMR (signal per million reads) normalization was performed on the read pileups.

Mononucleosomal DNA preparation:

For MNase-seq, 50□ml of synchronized meiotic cultures was harvested at T=3h and crosslinked with 1% formaldehyde for 30 minutes at room temperature. Crosslinking was quenched with 125□mM glycine, and cells were spheroplasted in Buffer Z (0.5□M sorbitol, 50□mM Tris-HCl pH□7.4, 10□mM β-mercaptoethanol) containing zymolyase. Spheroplasts were pelleted and resuspended in NP buffer (1□M sorbitol, 50□mM NaCl, 10□mM Tris-HCl pH□7.4, 5□mM MgCl□, 1□mM CaCl□, 0.5□mM spermidine, 1□mM β-mercaptoethanol, 0.075% NP-40) and digested with 5–80 units of micrococcal nuclease (MNase; Thermo Fisher Scientific, EN0181). MNase was diluted from a 300□U/µl stock to 20□U/µl, and mononucleosome-sized fragments were consistently obtained using 2□µl of a 1:4 dilution of this intermediate stock (10 units). Digestions were stopped with SDS and EDTA, followed by proteinase K treatment and overnight incubation at 65°C. Subsequent steps, including DNA purification and library preparation, were performed as described in [11]. Libraries were sequenced as 150-bp paired-end reads on an Illumina NextSeq 500, and the sequencing run was carried out by the Genomics Core at the New York University Center for Genomics and Systems Biology.

MNAse-seq data analysis:

To improve read alignment in repetitive subtelomeric regions, Bowtie 2 was configured to report multiple alignments using the “best match” mode as described for ChIP-seq. For signal quantification, fragments were processed with MACS2 (--nomodel --keep-dup all --SPMR) to generate normalized coverage tracks. To map MNase cleavage sites at nucleotide resolution, the 5’ end of each properly paired fragment was extracted from BAM files. This yielded single-base BED files representing MNase cut frequency, which were used for downstream metaplot analysis of nucleosome positioning.

Plug preparation for TrAEL-seq:

Plugs were prepared from meiotic cultures harvested 5 hours into meiosis to allow for accumulation of DSBs in the *dmc1* mutant background. For each strain, 20 ml of culture was pelleted and washed twice with CHEF TE buffer (10 mM Tris-HCl, pH 7.5, 50 mM EDTA, pH 8.0). The cell pellet was resuspended in 300 µl CHEF TE, followed by the addition of 4 µl zymolyase (10 mg/ml). The mixture was briefly vortexed and incubated at 42°C for approximately 30 seconds. Low-melting-point agarose (1% SeaPlaque GTG in 125 mM EDTA, pH 8.0), prewarmed to 42°C, was added and transferred into plug molds. Plugs were solidified on ice for 10 minutes before being transferred into LET buffer (10 mM Tris-HCl, pH 7.5; 0.5 M EDTA, pH 8.0). Plugs were incubated overnight at 37°C. The following day, plugs were treated with proteinase K in NDS buffer (10 mM Tris-HCl, pH 7.5; 0.5 M EDTA; 1% N-lauroylsarcosine) at 50°C overnight. After digestion, plugs were washed sequentially: first with CHEF TE for 1 hour at room temperature, followed by two washes with ice-cold CHEF TE containing 10 µl freshly prepared PMSF (100 mM) in ethanol, with each wash incubated for 1 hour in the cold room. A fourth wash was performed with RNase T1 in CHEF TE, incubated at 37°C for 1 hour, followed by a final wash with CHEF TE at room temperature for 1 hour. Plugs were stored at 4°C in CHEF TE until further use.

TrAEL-seq Library Preparation, Sequencing, and Data Analysis:

TrAEL-seq library preparation, sequencing and data analysis were conducted following the procedures outlined in [55]. TrAEL-seq signal pileups were generated using MACS2 (v2.2) and normalized pileups were generated using SPMR normalization. Downstream analyses were done in R. We note that telomeres can have free 3' ends that lead to a Spo11-independent TrAEL-seq signal. Because this signal showed strong batch effects that impacted the nearby Y' end X elements, we were unable to confidently analyze DSB formation in Y' and X elements using this method.

Statistical data analysis:

1) **Spike-in Normalization:** To allow for quantitative comparisons of chromatin immunoprecipitation (ChIP) enrichment between different strains or conditions, we performed spike-in normalization using the approach as previously published [36]. A known amount of SK288c chromatin (S288c strains engineered to efficiently enter meiosis) was used as a spike-in control, with sequence reads mapping to the S288c genome serving as a reference for normalizing sequencing depth and ChIP efficiency. The ratio of SK1 reads to S288c reads was then used to scale the enrichment values, allowing for direct comparison of protein abundance across different samples. This method is particularly useful for quantifying relative changes in protein occupancy between mutant and wild-type strains. Data sets from single strains, such as the analysis of wild-type strains presented in Figure 1, were analyzed without spike-in normalization, as this method is not necessary for such comparisons.

2) **Distance from telomeres plots:** The x-axis represents the distance from the annotated telomeric repeats, beginning at telomeres and extending inward. The y-axis indicates signal intensity, normalized so that the genome-wide average equals 1, or spike-in

normalized values where applicable. Data were processed as in [19] by binning signals into consecutive 200-bp windows, followed by kernel smoothing to minimize noise and highlight underlying trends.

3) **Bootstrapping plots:** Violin plots represent bootstrapped distributions obtained by performing 1000 iterations of resampling, where, for each iteration, 32 regions of 20 kb (or 16 regions for centromeric analyses) were sampled with replacement. The violin plots display the resulting distributions, indicating the median values along with two-sided 95% confidence intervals. Two-sided empirical p-values were computed against this distribution and BH-corrected. Effect sizes were measured via Cohen's d,

$$d = (\text{observed} - \mu_\text{boot})/\sigma_\text{boot}$$

where observed is the mean fold-enrichment in the focal regions; μ_boot is the mean of the bootstrap distribution of means; and σ_boot is the standard deviation of that bootstrap distribution.

4) **Meta gene analyses, and meta-X and Y' elements plots:** Only fully annotated X/Y' elements were analyzed; partially annotated copies were excluded because boundary-anchored profiles require accurate start and end coordinates. The excluded partial X elements are indicated with stars in **Supplementary Fig 2** (coordinates: VIII:9643-9820, X:15487-15645, XII:1020084-1020314, XV:1047720-1047878, XVI:9407-9565). Metagene analyses followed previously published approaches [13]. Similarly, to align variable-length X and Y' elements, we proportionally extended flanking regions based on the element length (100% extension for X elements and 50% for Y' elements, as indicated in the figure legends). Each extended region was then divided into 100 equal bins, scaling each element to fixed relative positions: X elements occupy the middle third (bins 33–66), and Y' elements occupy the middle half (bins 25–75). Signal intensities were averaged across these bins, ensuring proportional alignment at element

boundaries (e.g., bin 33 corresponds to the start of X elements, bin 25 corresponds to the start of Y' elements).

5) **Confidence bands vs. bootstrapping:** We used different approaches to determine significance depending on the structure of the underlying data. For metaplots of gene bodies, X, or Y' elements, the structure of the underlying sequences, and hence the distribution of chromatin marks and axis proteins, is relatively consistent after adjusting for the length of the elements. This structure allows meaningful confidence bands to be shown. By contrast, the distribution of axis binding sites is inherently sparse and differs between chromosome ends. As a result, a confidence band is not meaningful as the differences in location of axis sites would drown out consistent differences in signal across ends. To circumvent this problem, we instead combined the signal of the entire region and evaluated how significantly different the mean was from the rest of the chromosome using bootstrapping.

6) **Quantification of Red1 and Rec8 signals:** Rec8 peaks in **Fig. 4a** were derived from Rec8 ChIP-seq data in wild-type cells (the same dataset used in **Fig. 1b-f**). For each Rec8 peak region, the Red1 signal was calculated as the average score across the entire Rec8 peak interval. Peaks were annotated as centromere-proximal (±10 kb), telomere-proximal (20 kb), or non-centromere/non-telomere to contextualize their genomic distribution. If peak regions were straddling the boundaries, they were included as centromere-proximal/telomere-proximal. Straddling Peaks: Centromeres 0.16% and telomeres 0.08% of total peaks. We used Rec8 peaks because the Rec8 signal does not change significantly compared to genome average in the subtelomeric regions. The reduction of Red1 signal near telomeres means that some sites that have abundant Rec8 binding near telomeres do not have sufficient Red1 binding to be called as peaks.

7) **Quantification of Sir3 spreading from chromosome ends:** Sir3 spreading was quantified using a custom R pipeline. For each condition, ChIP-seq fold-enrichment over

input (FE) signals were extracted from chromosome-end regions from the X element toward the centromere. These regions were divided into consecutive 250 bp bins, and the average FE score was calculated for each bin. A dynamic threshold was defined as the upper bound of the 95% confidence interval of genome-wide FE values. Spreading was identified starting at the X-element boundary as the first continuous stretch of bins with FE scores above this threshold. The spreading region was considered to end when two consecutive bins fell below the threshold; the final bin above threshold before this drop marked the endpoint of Sir3 spreading. Spreading distances were aggregated across chromosome ends and visualized using violin plots.

8) **Promoter correlation plots:** Promoters were defined as the 250-bp window immediately upstream of annotated genes. Spo11-oligo signal was HPM-normalized and averaged per promoter in WT and *sir2Δ*. We plotted $\log_{10}$(*sir2Δ*/WT). To avoid inflated ratios from near-zero denominators, we set a data-driven floor at the 2nd percentile of promoter means pooled across WT and *sir2Δ* and excluded promoters only when both WT and *sir2Δ* means were below this floor (117 out of 5541; 2.11%). Results were robust to using a 5% floor (correlations changed only minimally). After filtering, the plotted set contained 34 genes within 5 kb of an X element (blue) and 5,356 other genes (red). The same promoter set was used for **Fig. 7f** and **Supplementary Fig. 9a–b**. RNA-seq fold changes were obtained with DESeq2 (two biological replicates per condition) and are shown as $\log_{10}$. Sir3 ChIP was genome-normalized (ChIP/Input). Values are means of two independent biological replicates and were reproducible between replicates.

9) **Hotspot calling in TrAEL-seq data:** DSB hotspots were identified from TrAEL-seq data using MACS2 (narrowPeak mode) on pooled biological replicates for each genotype, with the q-value (FDR) threshold set to control the false discovery rate. Hotspot totals were: *dmc1Δ* (n = 3,242), *sir3 dmc1Δ* (n = 3,224), *dot1Δ dmc1Δ* (n = 3,182), and *sir3*

dot1Δ dmc1Δ (n = 3,130). For quantification, signal was taken from MACS2 treat_pileup bedGraphs (RPM) and summarized as the mean RPM across each hotspot interval. For each telomere, the 0–20 kb region inward of the annotated X-element was tiled into 5-kb bins (bins 1–4 from the X element). Each hotspot was assigned to exactly one bin using its start coordinate, preventing double-counting of hotspots that span multiple bins.

Supporting information: Supplementary Figures and Tables are attached in a word document.

Data reporting: The datasets generated and analyzed in this paper, excluding published datasets, have been deposited in the Gene Expression Omnibus (GEO). The datasets can be accessed with the accession number for ChIP-seq: GSE287129 (reviewer access token: glgfkeugvjijjmh), for RNA-seq: GSE287127 (reviewer access token: stmnemakxzonxcp), and for TrAEL-seq: GSE287130 (reviewer access token: ehapywcoxrcbpab). Additionally, all ChIP-seq datasets used in this study are described in **Supplementary Table 3**, and all Spo11-oligo, RNA-seq and TrAEL-seq datasets are described in **Supplementary Table 4**.

Conflict of interest: The authors declare no conflicting interests.

Acknowledgements:

We thank Stephen P. Bell for generously providing the Sir3 antibody, N. Hollingsworth for the Red1 antibody, and A. Shinohara for the *hht1/2-K79R* strains. We also acknowledge the Genomics Core at the New York University Center for Genomics and Systems Biology for their valuable technical assistance and expertise in data processing. This work was supported in part by the NYU IT High-Performance Computing resources, services, and staff expertise. We are grateful to the Zegar Family Foundation for their generous support. TrAEL-seq library sequencing and processing were performed by the Genomics (Geno06) and Bioinformatics (Bioinf01) teams at the Babraham Institute, which receive financial support from the Institute

Core Capability Grant (BBSRC CCG). This research was financially supported as part of NIH grant R35 GM148223 to AH. ARR acknowledges support from a Fleur Strand Graduate Fellowship from the Department of Biology, as well as a Henry MacCracken Fellowship and a Dean's Dissertation Fellowship from the NYU Graduate School of Arts and Science. JH acknowledges funding from the BBSRC (BI Epigenetics ISP; BBS/E/B/000C0523), and KM acknowledges funding from the BBSRC (BB/W509917/1). The funders had no role in the preparation of this manuscript.

Author contributions: Conceptualization - A.R.R., V.V.S., H.G.B., and A.H; Investigation & Formal analysis - A.R.R., K.M., V.V.S., H.G.B., N.J.P., J.H., A.H; Computational Pipeline development - A.R.R.; Manuscript writing (initial draft) - A.R.R. and A.H.; Manuscript editing - all authors.

Figures:

Figure 1: Distinct axis-protein enrichment patterns at chromosome ends.

(a) Schematic of chromosome-end architecture in *S. cerevisiae*. XY′ ends contain Y′ elements; X-only ends lack Y′ elements. We define the subtelomeric domains as encompassing the last 20 kb from chromosome ends; they thus also encompass any X or Y' elements. The adjacent EARs extend 20-120kb from ends. **(b)** Mean enrichment of Rec8 (light blue), Red1 (red), and Hop1 (purple) versus distance from telomeres in wild type (WT) early prophase I (T=3h) from published data [16,19,36], normalized to a genome average of 1 (gray dashed line; see Methods: Distance from telomeres plots). Range of the subtelomeric domains (SubTel) is indicated with a solid grey line, EARs are indicated with an orange line. **(c)** Genome-wide bootstrap distributions of fold-enrichment (32 × 20-kb windows; n = 1,000 resamples; see Methods: Bootstrapping plots). Grey dashed line is genome average. Black lines show medians and 95% CIs; orange/red circles mark the observed mean in the last 20 kb. Two-sided empirical test with

Benjamini-Hochberg (BH) correction, effect sizes via Cohen's d (negative = depletion at ends relative to the genome-wide null): Hop1 ($p = 0.001$; BH = 0.0015; $d = -3.51$); Red1 ($p < 1x10^{-6}$; BH < 1×10^{-6}; $d = -5.23$); Rec8 ($p = 0.368$; BH = 0.368; $d = -0.89$). **(d)** Metaplots anchored at X elements, stratified by end class. Only fully annotated X elements were used (X-only, n = 7; XY′, n = 20). Flanks scaled to element length (X: 100% each side). Grey dashed line is genome average, vertical dotted lines mark X boundaries; shaded bands indicate 95% confidence intervals (CI; see Methods: Meta gene analyses, and meta-X and Y' elements plots). **(e)** Axis protein ChIP signal (Hop1, Red1, Rec8) at X elements on X-only versus XY′ ends. Values represent the mean ChIP/input signal per X element. Box-and-whisker plots show the distribution across elements. Two-sided unpaired Student's t-tests with BH correction; stars reflect BH-adjusted p (* ≤ 0.05; n.s., not significant). Statistics (per X element; Cohen's d; positive = higher at X-only): Hop1 ($p = 0.0186$; BH = 0.0186; $d = 1.13$); Red1 ($p = 0.0058$; BH = 0.0118; $d = 1.77$); Rec8 ($p = 0.0079$; BH = 0.0118; $d = 1.62$). **(f)** Metaplot anchored at Y′ elements. Only fully annotated Y′ were analyzed and flanks were scaled to 50% of Y′ length. Blue arrow indicates Y′-ORF orientation. Grey dashed line is genome average and vertical dotted lines mark Y′ boundaries. Shaded bands are 95% CIs (see Methods: Meta gene analyses, and meta-X and Y' elements plots). Averages of two biological replicates.

Figure 2: Multiple *cis*-acting features correlated with axis-protein depletion near telomeres.

(a) Distance-from-telomere metaplots of Rec8, Hop1, and Red1 ChIP enrichment (ChIP/Input) at XY′ ends (n = 21) and X-only ends (n = 11). Dashed gray line, genome-wide mean set to 1. WT early prophase I datasets (T=3h) from [16,19,36] (see Methods: Distance from telomeres plots). **(b)** Red1 binding (T=4h) along telomere-proximal arms in SK1/S288C hybrids (chrIV-R and chrI-L), using data from [39]. Tracks are shown for unfused (WT) and chrIV/I fused strains homozygous or heterozygous for *cen1Δ* or *cen4Δ* (colors as indicated). Vertical dashed black

line indicates engineered fusion sites. The plot only includes points common to all datasets, which is why the WT unfused data in the regions between the telomeres and the fusion sites are missing. Blue and green bars indicate X and Y′ elements that were deleted in the process of fusing the chromosomes. Thin lines are genome-normalized Red1 tracks; thick lines are loess-smoothed overlays for trends (span = 1). Circle indicates *CEN1*. The dip in signal on the right side of chrI-L is because of deletion of *CEN1* in some of the strains as previously described [39]. **(c)** Red1 distance-from-telomere metaplot comparing chrIV/I fused arms (homozygous + heterozygous; SK1 and S288C) to unfused arms. Thin lines show group-means; thick lines show loess-smoothed overlays (span = 1). The dip in signal on the right side of the fused graph is because of deletion of *CEN1* in some of the strains as previously described [39]. Note that the underlying data is sparser on the telomere-proximal side because of differences in fusion site locations. Coding density is shown as loess-smoothed line (span = 1) with yellow dots indicating raw means of 10-kb windows. Coding density is defined as the fraction of nucleotides overlapping an annotated ORF. **(d)** Coding density versus distance from telomeres overlaid on axis-protein metaplots. Yellow points show mean coding density in 10-kb bins, plotted at bin midpoints (right y-axis). Black line connects the dots for easier visualization of trend. **(e)** Relationship between coding density and mean Red1 enrichment. Scatter plots show non-overlapping 20-kb bins at dots. "Y′ masked" means Y′ sequence is excluded from both measurements (we mask Y′ bases when tallying coding density and when averaging Red1; bins that are entirely Y′ are excluded). Panels show Last 20 kb, EARs (20–120 kb), and the rest of the genome. Black lines are least-squares fits, with 95% CIs shown in grey. Pearson r values are indicated.

Figure 3: Differential recruitment of Red1 at chromosome ends by Rec8-dependent and -independent pathways.

(a) Distance-from-telomere profiles of Red1 (spike-in normalized; see Methods) in WT, *rec8*, *hop1-phd*, and *hop1-phd rec8* during early prophase I (3 h) using published data [13,15] (see Methods: Distance from telomeres plots). Colored dashed lines mark each strain's genome-wide mean after spike-in scaling. Ranges of subtelomeric domains (grey) and EARs (orange) are indicated above the plot. **(b)** Genome-wide bootstrap distributions of fold-enrichment (32 × 20-kb windows; n = 1,000 resamples; see Methods: Bootstrapping plots). Black lines show medians and 95% CIs; orange/red circles mark the observed means in the last 20 kb. Two-sided empirical tests with BH correction; Cohen's d (negative = depletion at ends): WT ($p < 1x10^{-6}$; BH $< 1x10^{-6}$; d = −5.23); *hop1-phd* ($p < 1x10^{-6}$; BH $< 1x10^{-6}$; d = −7.85); *rec8* (p = 0.001; BH = 0.0013; d = 3.54); *hop1-phd rec8* (p = 0.059; BH = 0.059; d = 1.87). **(c-d)** Meta-X and Y' elements plots at chromosome ends. X elements were stratified by end class and only fully annotated X elements were used (X-only, n = 7; XY′, n = 20) with flanks scaled to 100% of X length. Y′ elements use flanks scaled to 50% of Y′ length. Blue arrow indicates Y′-ORF orientation. Shaded bands show two-sided 95% CIs (see Methods: Meta gene analyses, and meta-X and Y' elements plots). Averages of two biological replicates.

Figure 4: Dot1 shapes axis-protein distribution at chromosome ends and chromosome interiors.

(a) Mean Red1 vs Rec8 enrichment at Rec8 peaks, split by region (terminal 20 kb, centromeres ±10 kb, interior) using published data [16]. Global fit (purple) and region-specific fits (green dashes). Slope comparisons (two-sided Student's t-tests; BH-adjusted): interior vs telomeres ($p = 3.43x10^{-19}$; BH $= 5.14x10^{-19}$); interior vs pericentromeres ($p = 3.12x10^{-24}$; BH $= 9.36\times10^{-24}$); telomeres vs pericentromeres (p = 0.525; BH = 0.525). stars reflect BH-adjusted p (*** ≤ 0.001; n.s., not significant) (See Methods: Quantification of Red1 and Rec8 signals). **(b)** Mean enrichment of H4K44ac and H3K56ac [44], H3K4me3 [45], and H3K79me3 versus distance from telomeres, each normalized to H3 or H4 (see Methods: Distance from telomeres plots). **(c)**

Spike-in–normalized Red1 distance profiles in WT, *dot1Δ*, and *set1Δ*. Data from [36]. See Methods: Distance from telomeres plots. Note that *set1Δ* mutants are somewhat less synchronous because of delays in premeiotic DNA replication. **(d-e)** Meta-X and Y' elements plots of Red1 enrichment in WT (red), *dot1Δ* (yellow) and *set1Δ* mutants (purple). X elements stratified by end class and only fully annotated X elements were used (X-only, n = 7; XY′, n = 20) with flanks scaled to 100% of X length. Y′ elements use flanks scaled to 50% of Y′ length. Blue arrow indicates Y′-ORF orientation. Shaded bands show two-sided 95% CIs (see Methods: Meta gene analyses, and meta-X and Y' elements plots). **(f)** Region-stratified Red1 enrichment profiles in WT (pink) and *dot1Δ* mutants (yellow) across intergenic (left) and genic (right) sequences versus distance from telomeres. Averages of two biological replicates.

Figure 5: H3K79-independent activity of Dot1 reduces axis proteins near chromosome ends.

(a) Distance-from-telomere profiles of Red1 enrichment (spike-in normalized) in WT, *dot1Δ,* and *hht1/2-K79R* during early prophase I (3 h; see Methods, Distance from telomeres plots). WT and *dot1Δ* data are the same as in **Figure 4c**. **(b)** Genome-wide bootstrap distributions (32 × 20-kb windows; n = 1,000 resamples) of Red1 enrichment. Black lines show medians and two-sided 95% CIs; orange/red circles mark the observed mean in the terminal 20 kb. Two-sided empirical test, with BH correction; effect sizes via Cohen's d: WT (p = 0.0020; BH = 0.0030; d = −4.09); *dot1Δ* (p = 0.180; BH = 0.180; d = −1.30); *hht1/2-K79R* (p = 0.0010; BH = 0.0030; d = −6.24). **(c-d)** Meta-X and Y' elements plots at chromosome ends. X elements stratified by end class and only fully annotated X elements were used (X-only, n = 7; XY′, n = 20) with flanks scaled to 100% of X length. Y′ elements use flanks scaled to 50% of Y′ length. Blue arrow indicates Y′-ORF orientation. Shaded bands show two-sided 95% CIs (see Methods: Meta gene analyses, and meta-X and Y' elements plots). Averages of two biological replicates.

Figure 6: Effects of Dot1 on axis-protein deposition depend on Sir3.

(a) Distance-from-telomere profiles of Red1 enrichment (spike-in normalized) in WT, *dot1Δ*, *sir3*, and *sir3 dot1Δ* during early prophase I (3 h; see Methods, Distance from telomeres plots). **(b)** Genome-wide bootstrap distributions (32 × 20-kb windows; n = 1,000 resamples) of Red1 enrichment. Black lines show medians and two-sided 95% CIs; orange/red circles mark the observed mean in the terminal 20 kb. Two-sided empirical test, with BH correction; effect sizes via Cohen's d: WT (p = 0.002; BH = 0.003; d = −4.09); *dot1Δ* (p = 0.18; BH = 0.18; d = −1.30); *sir3* (p = 0.001; BH = 0.002; d = −5.87); *sir3 dot1Δ* (p = 0.001; BH = 0.002; d = −6.50). **(c-d)** Meta-X and Y' elements plots at chromosome ends. X elements stratified by end class and only fully annotated X elements were used (X-only, n = 7; XY′, n = 20) with flanks scaled to 100% of X length. Y′ elements use flanks scaled to 50% of Y′ length. Blue arrow indicates Y′-ORF orientation. Shaded bands show two-sided 95% CIs (see Methods: Metagene analyses, and meta-X and Y' elements plots). Averages of two biological replicates.

Figure 7: Sir3 occupancy relates to local transcription and MNase accessibility near chromosome ends.

(a) Metaplots anchored at X elements, stratified by end class and only fully annotated X elements were used (X-only, n = 7; XY′, n = 21). Flanks scaled to element length (X: 100% each side). Vertical dotted lines mark X boundaries. Shaded bands indicate 95% CIs (see Methods: Metagene analyses, and meta-X and Y' elements plots). **(b)** Sir3 ChIP signal at X elements on X-only versus XY′ ends during mid-log, meiotic induction (T=0h), and meiotic prophase (T=3h). Values represent the mean ChIP/input signal per X element. Box-and-whisker plots show the distribution across elements. Two-sided unpaired Student's t-tests with BH correction; stars reflect BH-adjusted p (** ≤ 0.01). Statistics (per X element; Cohen's d; negative = lower at XY′): mid-log (p = 0.007; BH = 0.007; d = −1.22); T=0 (p = 0.007; BH = 0.007; d = −1.32); T=3 h (p = 0.002; BH = 0.006; d = −1.11). **(c)** Metaplot anchored at Y′ elements. Fully annotated Y′ only;

flanks scaled to 50% of Y′ length. Vertical dotted lines mark Y′ boundaries. Blue arrow indicates Y′-ORF orientation. Shaded bands show 95% CIs (see Methods: Metagene analyses, and meta-X and Y' elements plots). **(d-e)** Example Sir3 ChIP-seq tracks on chr VII-L and chr VI-L at mid-log and T=3 h. Curves show ChIP/Input. Positions of X elements, Y' elements and ORFs are indicated (inset white triangle shows ORF orientation). **(f)** mRNA-seq fold change (*sir3*/WT, log10) at T=3h versus average Sir3 ChIP enrichment in the 250 bp upstream of ORFs. **(g)** MNase-seq fragment frequency (RPM/kb) at T=3h versus distance from telomeres (0–40 kb) for WT, *dot1Δ*, *sir3*, and *sir3 dot1Δ.* All experiments: averages of two biological replicates.

Figure 8: Sir influences DSB formation near chromosome ends.

(a) Boxplots of log10 Spo11-oligo signal (hits per million) at X and Y′ elements in WT and *sir2Δ*, from published datasets [19,74]. Points are element scores; gray lines connect matched elements across strains. Two-sided Wilcoxon rank-sum tests with BH correction; effect sizes are rank-biserial r (positive = higher in *sir2Δ*). X elements: ($p = 7.9 \times 10^{-4}$, BH = 1.6×10^{-3}); r = 0.83), Y′ elements: (p = 0.127; BH = 0.127; r = 0.32). Stars reflect BH-adjusted p (** ≤ 0.01; n.s., not significant). **(b)** TrAEL-seq hotspot intensity per 5-kb bin as a function of distance from X elements. Log10 average peak intensity (RPM) for peaks in each bin in *dmc1Δ*, *sir3 dmc1Δ, dot1Δ dmc1Δ*, and *sir3 dot1Δ dmc1Δ* (see Methods, TrAEL-seq hotspot calling and quantification). Per-bin two-sided Wilcoxon rank-sum tests contrasting (*sir3 dmc1Δ* + *sir3 dot1Δ dmc1Δ*) vs (*dmc1Δ* + *dot1Δ dmc1Δ*), BH-corrected across bins; effect sizes are rank-biserial (positive = higher in *sir3* mutants. Bin 1: p = 3.15 x 10-7; BH = 1.26 x 10-6; r = 0.67. Bin 2: p = 0.237; BH = 0.474; r = 0.13. Bin 3: p = 0.527; BH = 0.703; r = 0.07. Bin 4: p = 0.823; BH = 0.823; r = 0.02. Stars reflect BH-adjusted p (*** ≤ 0.001; n.s., not significant). **(c)** Mean hotspot counts per 5-kb bin as a function of distance from X elements for the indicated strains. Hotspots were identified from TrAEL-seq peak calls. Because most telomere-proximal bins contained only 0-2 hotspots, the data had too few discrete steps for box or violin blots. Therefore, the means of

the data are shown as a bar plot (error bars: SEM). Per-bin two-sided Wilcoxon rank-sum tests contrasting (*sir3 dmc1Δ* + sir3 *dot1Δ dmc1Δ*) vs (*dmc1Δ* + *dot1Δ dmc1Δ*), BH-corrected across bins; effect sizes are rank-biserial (positive = higher in *sir3* mutants. Bin 1: raw p = 5.63×10^{-3}; BH = 2.25×10^{-2}; r = 0.24. Bin 2: raw p = 0.376; BH = 0.752; r = 0.08. Bin 3: raw p = 0.687; BH = 0.915; r = 0.04. Bin 4: raw p = 0.920; BH = 0.920; r = 0.01. Stars reflect BH-adjusted p (* ≤ 0.05; n.s., not significant). **(d)** TrAEL-seq (colored) and MNase-seq (gray) tracks at a representative subtelomeric region (chrV-R) for *dmc1Δ*, *sir3 dmc1Δ, dot1Δ dmc1Δ*, and *sir3 dot1Δ dmc1Δ*. Black arrow indicates a cryptic DSB hotspot that becomes active in the absence of *SIR3*. Grey arrow indicates an unusual Y'-associated hotspot that becomes stronger in the absence of *SIR3.* Other Y' elements generally do not exhibit altered TrAEL-seq signal. **(e)** TrAEL-seq meta-plots showing mean DSB signal (reads per million) as a function of distance from X elements in the strains indicated. Ranges of subtelomeric domains (grey) and EARs (orange) are indicated above the plot.

References:

1 Mozzachiodi, S. & Liti, G. Evolution of yeast hybrids by aborted meiosis. *Current Opinion in Genetics and Development* **77**, 101980-101980 (2022). https://doi.org/10.1016/j.gde.2022.101980

2 Börner, G. V., Hochwagen, A. & MacQueen, A. J. Meiosis in budding yeast. *Genetics* **225**, 1-33 (2023). https://doi.org/10.1093/genetics/iyad125

3 Duro, E. & Marston, A. L. From equator to pole: Splitting chromosomes in mitosis and meiosis. *Genes and Development* **29**, 109-122 (2015). https://doi.org/10.1101/gad.255554.114

4 Hunter, N. Meiotic recombination: The essence of heredity. *Cold Spring Harbor Perspectives in Biology* **7** (2015). https://doi.org/10.1101/cshperspect.a016618

5 Arter, M. & Keeney, S. Divergence and conservation of the meiotic recombination machinery. *Nature Reviews Genetics* **25**, 309-325 (2024). https://doi.org/10.1038/s41576-023-00669-8

6 Lichten, M. Meiotic chromatin: The substrate for recombination initiation. *Genome Dynamics and Stability* **3**, 165-193 (2008). https://doi.org/10.1007/7050_2008_040

7 Ito, M. & Shinohara, A. Chromosome architecture and homologous recombination in meiosis. *Frontiers in Cell and Developmental Biology* **10**, 1097446 (2022). https://doi.org/10.3389/fcell.2022.1097446

8 Raghavan, A. R. & Hochwagen, A. Keeping it safe: control of meiotic chromosome breakage. *Trends in Genetics* (2024). https://doi.org/https://doi.org/10.1016/j.tig.2024.11.006

9 Zhang, K., Wu, X. C., Zheng, D. Q. & Petes, T. D. Effects of Temperature on the Meiotic Recombination Landscape of the Yeast *Saccharomyces cerevisiae*. *mBio* **8** (2017). https://doi.org/10.1128/mBio.02099-17

10 Mohibullah, N. & Keeney, S. Numerical and spatial patterning of yeast meiotic DNA breaks by Tel1. *Genome Research* **27** (2017). https://doi.org/10.1101/gr.213587.116

11 Pan, J. *et al.* A hierarchical combination of factors shapes the genome-wide topography of yeast meiotic recombination initiation. *Cell* **144**, 719-731 (2011). https://doi.org/10.1016/j.cell.2011.02.009

12 Panizza, S. *et al.* Spo11-accessory proteins link double-strand break sites to the chromosome axis in early meiotic recombination. *Cell* **146**, 372-383 (2011). https://doi.org/10.1016/j.cell.2011.07.003

13 Heldrich, J. *et al.* Two pathways drive meiotic chromosome axis assembly in *Saccharomyces cerevisiae*. *Nucleic Acids Research* **50**, 4545-4556 (2022).

14 Joshi, N., Barot, A., Jamison, C. & Börner, G. V. Pch2 links chromosome axis remodeling at future crossover sites and crossover distribution during yeast meiosis. *PLoS Genetics* **5**, e1000557 (2009). https://doi.org/10.1371/journal.pgen.1000557

15 Milano, C. R. *et al.* Chromatin binding by HORMAD proteins regulates meiotic recombination initiation. *EMBO Journal* **43**, 836-867 (2024). https://doi.org/10.1038/s44318-024-00034-3

16 Sun, X. *et al.* Transcription dynamically patterns the meiotic chromosome-axis interface. *eLife* **4**, 1-23 (2015). https://doi.org/10.7554/eLife.07424

17 Blitzblau, H. G., Bell, G. W., Rodriguez, J., Bell, S. P. & Hochwagen, A. Mapping of Meiotic Single-Stranded DNA Reveals Double-Strand-Break Hotspots near Centromeres and Telomeres. *Current Biology* **17**, 2003-2012 (2007). https://doi.org/10.1016/j.cub.2007.10.066

18 Mancera, E., Bourgon, R., Brozzi, A., Huber, W. & Steinmetz, L. M. High-resolution mapping of meiotic crossovers and non-crossovers in yeast. *Nature* **454**, 479-485 (2008). https://doi.org/10.1038/nature07135

19 Subramanian, V. V. *et al.* Persistent DNA-break potential near telomeres increases initiation of meiotic recombination on short chromosomes. *Nature Communications* **10**, 1-15 (2019). https://doi.org/10.1038/s41467-019-08875-x

20 Barton, A. B., Su, Y., Lamb, J., Barber, D. & Kaback, D. B. A function for subtelomeric DNA in *Saccharomyces cerevisiae*. *Genetics* **165**, 929-934 (2003). https://doi.org/10.1093/genetics/165.2.929

21 Sasaki, M., Lange, J. & Keeney, S. Genome destabilization by homologous recombination in the germ line. *Nature Reviews Molecular Cell Biology* **11**, 182-195 (2010). https://doi.org/10.1038/nrm2849

22 Ross, L. O., Maxfield, R. & Dawson, D. Exchanges are not equally able to enhance meiotic chromosome segregation in yeast. *PNAS* **93** (1996). https://doi.org/10.1073/pnas.93.10.4979

23 Ghosh, S., Feingold, E. & Dey, S. K. Etiology of Down syndrome: Evidence for consistent association among altered meiotic recombination, nondisjunction, and maternal age across populations. *American Journal of Medical Genetics, Part A* **149a**, 1415-1420 (2009). https://doi.org/10.1002/ajmg.a.32932

24 Lamb, N. E., Yu, K., Shaffer, J., Feingold, E. & Sherman, S. L. Association between maternal age and meiotic recombination for trisomy 21. *American Journal of Human Genetics* **76**, 91-99 (2005). https://doi.org/10.1086/427266

25 Louis, E. J. The chromosome ends of *Saccharomyces cerevisiae*. *Yeast* **11**, 1553-1573 (1995). https://doi.org/10.1002/yea.320111604

26 Pryde, F. E., Gorham, H. C. & Louis, E. J. Chromosome ends: all the same under their caps. *Current Opinion in Genetics and Development* **7**, 822-828 (1997). https://doi.org/10.1016/s0959-437x(97)80046-9

27 Fabre, E. & Spichal, M. in *Subtelomeres* (eds Edward J. Louis & Marion M. Becker) 13-37 (Springer Berlin Heidelberg, 2014).

28 Hocher, A. & Taddei, A. Subtelomeres as Specialized Chromatin Domains. *BioEssays* **42** (2020). https://doi.org/10.1002/bies.201900205

29 Brothers, M. & Rine, J. Distinguishing between recruitment and spread of silent chromatin structures in *Saccharomyces cerevisiae*. *eLife* **11**, 1-23 (2022). https://doi.org/10.7554/eLife.75653

30 Hocher, A. *et al.* Expanding heterochromatin reveals discrete subtelomeric domains delimited by chromatin landscape transitions. *Genome Research* **28**, 1852-1866 (2018). https://doi.org/10.1101/gr.236554.118

31 Gerton, J. L. *et al.* Global mapping of meiotic recombination hotspots and coldspots in the yeast *Saccharomyces cerevisiae*. *PNAS* **97**, 11383-11390 (2000). https://doi.org/10.1073/pnas.97.21.11383

32 Buhler, C., Borde, V. & Lichten, M. Mapping meiotic single-strand DNA reveals a new landscape of DNA double-strand breaks in *Saccharomyces cerevisiae*. *PLoS Biology* **5**, 2797-2808 (2007). https://doi.org/10.1371/journal.pbio.0050324

33 Murakami, H. *et al.* Multilayered mechanisms ensure that short chromosomes recombine in meiosis. *Nature* (2020). https://doi.org/10.1038/s41586-020-2248-2

34 D'Angiolo, M. *et al.* Telomeres are shorter in wild *Saccharomyces cerevisiae* isolates than in domesticated ones. *Genetics* **223** (2023). https://doi.org/10.1093/genetics/iyac186

35 Yue, J. X. *et al.* Contrasting evolutionary genome dynamics between domesticated and wild yeasts. *Nature Genetics* **49**, 913-924 (2017). https://doi.org/10.1038/ng.3847

36 Vale-Silva, L. A., Markowitz, T. E. & Hochwagen, A. SNP-ChIP: A versatile and tag-free method to quantify changes in protein binding across the genome. *BMC Genomics* **20**, 1-10 (2019). https://doi.org/10.1186/s12864-018-5368-4

37 Kwapisz, M. & Morillon, A. Subtelomeric Transcription and its Regulation. *Journal of molecular biology* **432**, 4199-4219 (2020). https://doi.org/10.1016/j.jmb.2020.01.026

38 Wellinger, R. J. & Zakian, V. A. Everything you ever wanted to know about *Saccharomyces cerevisiae* telomeres: Beginning to end. *Genetics* **191**, 1073-1105 (2012). https://doi.org/10.1534/genetics.111.137851

39 Luo, J. *et al.* Synthetic chromosome fusion: Effects on mitotic and meiotic genome structure and function. *Cell Genomics* **3** (2023). https://doi.org/10.1016/j.xgen.2023.100439

40 Glynn, E. F. *et al.* Genome-wide mapping of the cohesin complex in the yeast *Saccharomyces cerevisiae*. *PLoS Biology* **2** (2004). https://doi.org/10.1371/journal.pbio.0020259

41 Bausch, C. *et al.* Transcription Alters Chromosomal Locations of Cohesin in *Saccharomyces cerevisiae*. *Molecular and Cellular Biology* **27**, 8522-8532 (2007). https://doi.org/10.1128/MCB.01007-07

42 Ocampo-Hafalla, M. T. & Uhlmann, F. Cohesin loading and sliding. *Journal of Cell Science* **124**, 685-691 (2011). https://doi.org/10.1242/jcs.073866

43 Borde, V. *et al.* Histone H3 lysine 4 trimethylation marks meiotic recombination initiation sites. *EMBO Journal* **28**, 99-111 (2009). https://doi.org/10.1038/emboj.2008.257

44 Hu, J. *et al.* H4K44 Acetylation Facilitates Chromatin Accessibility during Meiosis. *Cell Reports* **13**, 1772-1780 (2015). https://doi.org/10.1016/j.celrep.2015.10.070

45 Zhu, X. & Keeney, S. High-resolution global analysis of the influences of Bas1 and Ino4 transcription factors on meiotic DNA break distributions in *Saccharomyces cerevisiae*. *Genetics* **201**, 525-542 (2015). https://doi.org/10.1534/genetics.115.178293

46 Bani Ismail, M., Shinohara, M. & Shinohara, A. Dot1-dependent histone H3K79 methylation promotes the formation of meiotic double-strand breaks in the absence of histone H3K4 methylation in budding yeast. *PLoS ONE* **9** (2014). https://doi.org/10.1371/journal.pone.0096648

47 Shilatifard, A. Chromatin modifications by methylation and ubiquitination: Implications in the regulation of gene expression. *Annual Review of Biochemistry* **75**, 243-269 (2006). https://doi.org/10.1146/annurev.biochem.75.103004.142422

48 Takahashi, Y.-H. *et al.* Dot1 and Histone H3K79 Methylation in Natural Telomeric and HM Silencing. *Molecular Cell* **42**, 118-126 (2011). https://doi.org/10.1016/j.molcel.2011.03.006

49 Hoppe, G. J. *et al.* Steps in Assembly of Silent Chromatin in Yeast: Sir3-Independent Binding of a Sir2/Sir4 Complex to Silencers and Role for Sir2-Dependent Deacetylation. *Molecular and Cellular Biology* **22**, 4167-4180 (2002). https://doi.org/10.1128/MCB.22.12.4167-4180.2002

50 Rusche, L. N., Kirchmaier, A. L. & Rine, J. The Establishment, Inheritance, and Function of Silenced Chromatin in *Saccharomyces cerevisiae*. *Annual Review of Biochemistry* **72**, 481-516 (2003). https://doi.org/10.1146/annurev.biochem.72.121801.161547

51 Pryde, F. E. & Louis, E. J. Limitations of silencing at native yeast telomeres. *EMBO Journal* **18**, 2538-2550 (1999). https://doi.org/10.1093/emboj/18.9.2538

52 Gartenberg, M. R. & Smith, J. S. The Nuts and Bolts of Transcriptionally Silent Chromatin in *Saccharomyces cerevisiae*. *Genetics* **203**, 1563-1599 (2016). https://doi.org/10.1534/genetics.112.145243

53 Hediger, F., Neumann, F. R., Van Houwe, G., Dubrana, K. & Gasser, S. M. Live imaging of telomeres: yKu and Sir proteins define redundant telomere-anchoring pathways in yeast. *Current Biology* **12**, 2076-2089 (2002). https://doi.org/10.1016/s0960-9822(02)01338-6

54 Mieczkowski, P. A., Dominska, M., Buck, M. J., Lieb, J. D. & Petes, T. D. Loss of a histone deacetylase dramatically alters the genomic distribution of Spo11p-catalyzed DNA breaks in *Saccharomyces cerevisiae*. *PNAS* **104**, 3955-3960 (2007). https://doi.org/10.1073/pnas.0700412104

55 Kara, N., Krueger, F., Rugg-Gunn, P. & Houseley, J. Genome-wide analysis of DNA replication and DNA double-strand breaks using TrAEL-seq. *PLoS Biology* **19** (2021). https://doi.org/10.1371/journal.pbio.3000886

56 Bishop, D. K., Park, D., Xu, L. & Kleckner, N. *DMC1*: A meiosis-specific yeast homolog of E. coli *recA* required for recombination, synaptonemal complex formation, and cell cycle progression. *Cell* **69**, 439-456 (1992). https://doi.org/10.1016/0092-8674(92)90446-J

57 Vader, G. *et al.* Protection of repetitive DNA borders from self-induced meiotic instability. *Nature* **477**, 115-121 (2011). https://doi.org/10.1038/nature10331

58 Blitzblau, H. G., Chan, C. S., Hochwagen, A. & Bell, S. P. Separation of DNA replication from the assembly of break-competent meiotic chromosomes. *PLoS Genetics* **8**, e1002643 (2012). https://doi.org/10.1371/journal.pgen.1002643

59 Stulemeijer, I. J. *et al.* Dot1 binding induces chromatin rearrangements by histone methylation-dependent and -independent mechanisms. *Epigenetics and Chromatin* **4**, 2 (2011). https://doi.org/10.1186/1756-8935-4-2

60 Lee, S. *et al.* Dot1 regulates nucleosome dynamics by its inherent histone chaperone activity in yeast. *Nature Communications* **9**, 240 (2018). https://doi.org/10.1038/s41467-017-02759-8

61 San-Segundo, P. A. & Roeder, G. S. Role for the Silencing Protein Dot1 in Meiotic Checkpoint Control. 3601-3615 (2000).

62 Wood, K., Tellier, M. & Murphy, S. DOT1L and H3K79 Methylation in Transcription and Genomic Stability. *Biomolecules* **8** (2018). https://doi.org/10.3390/biom8010011

63 Lam, I. & Keeney, S. Nonparadoxical evolutionary stability of the recombination initiation landscape in yeast. *Science* **350**, 932-937 (2015). https://doi.org/10.1126/science.aad0814

64 Choi, K. *et al.* Nucleosomes and DNA methylation shape meiotic DSB frequency in *Arabidopsis thaliana* transposons and gene regulatory regions. *Genome Research* **28**, 532-546 (2018). https://doi.org/10.1101/gr.225599.117

65 He, F. *et al.* SESAME-catalyzed H3T11 phosphorylation inhibits Dot1-catalyzed H3K79me3 to regulate autophagy and telomere silencing. *Nature Communications* **13**, 7526 (2022). https://doi.org/10.1038/s41467-022-35182-9

66 Su, Y., Barton, A. B. & Kaback, D. B. Decreased meiotic reciprocal recombination in subtelomeric regions in *Saccharomyces cerevisiae*. *Chromosoma* **109**, 467-475 (2000). https://doi.org/10.1007/s004120000098

67 Humphryes, N. & Hochwagen, A. A non-sister act: Recombination template choice during meiosis. *Experimental Cell Research* **329**, 53-60 (2014). https://doi.org/10.1016/j.yexcr.2014.08.024

68 Scherthan, H. A bouquet makes ends meet. *Nature Reviews Molecular Cell Biology* **2**, 621-627 (2001). https://doi.org/10.1038/35085086

69 Medhi, D., Goldman, A. S. & Lichten, M. Local chromosome context is a major determinant of crossover pathway biochemistry during budding yeast meiosis. *eLife* **5**, e19669 (2016). https://doi.org/10.7554/eLife.19669.001

70 Langmead, B. & Salzberg, S. L. Fast gapped-read alignment with Bowtie 2. *Nature Methods* **9**, 357-359 (2012). https://doi.org/10.1038/nmeth.1923

71 Kar, F. M., Vogel, C. & Hochwagen, A. Meiotic DNA breaks activate a streamlined phospho-signaling response that largely avoids protein-level changes. *Life Science Alliance* **5**, 1-15 (2022). https://doi.org/10.26508/LSA.202201454

72 Ewels, P. A. P. A. F. S. & et al. The nf-core framework for community-curated bioinformatics pipelines. *Nature Biotechnology* **38**, 271-271 (2020). https://doi.org/10.1038/s41587-020-0435-1

73 Patro, R., Duggal, G., Love, M. I., Irizarry, R. A. & Kingsford, C. Salmon provides fast and bias-aware quantification of transcript expression. *Nature Methods* **14**, 417-419 (2017). https://doi.org/10.1038/nmeth.4197

74 Thacker, D., Mohibullah, N., Zhu, X. & Keeney, S. Homologue engagement controls meiotic DNA break number and distribution. *Nature* **510**, 241-246 (2014). https://doi.org/10.1038/nature13120

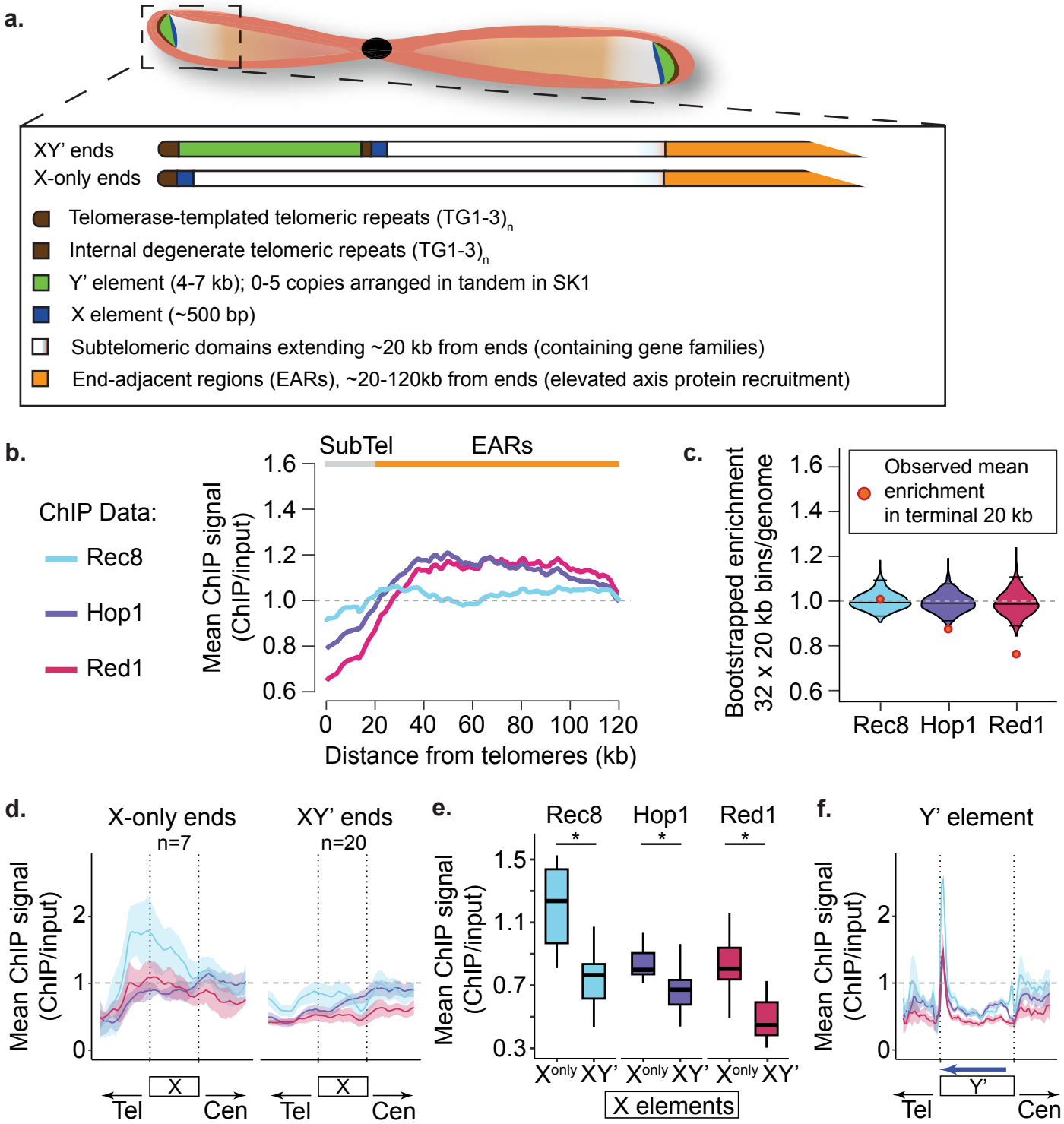

Raghavan *et al*, Fig. 1

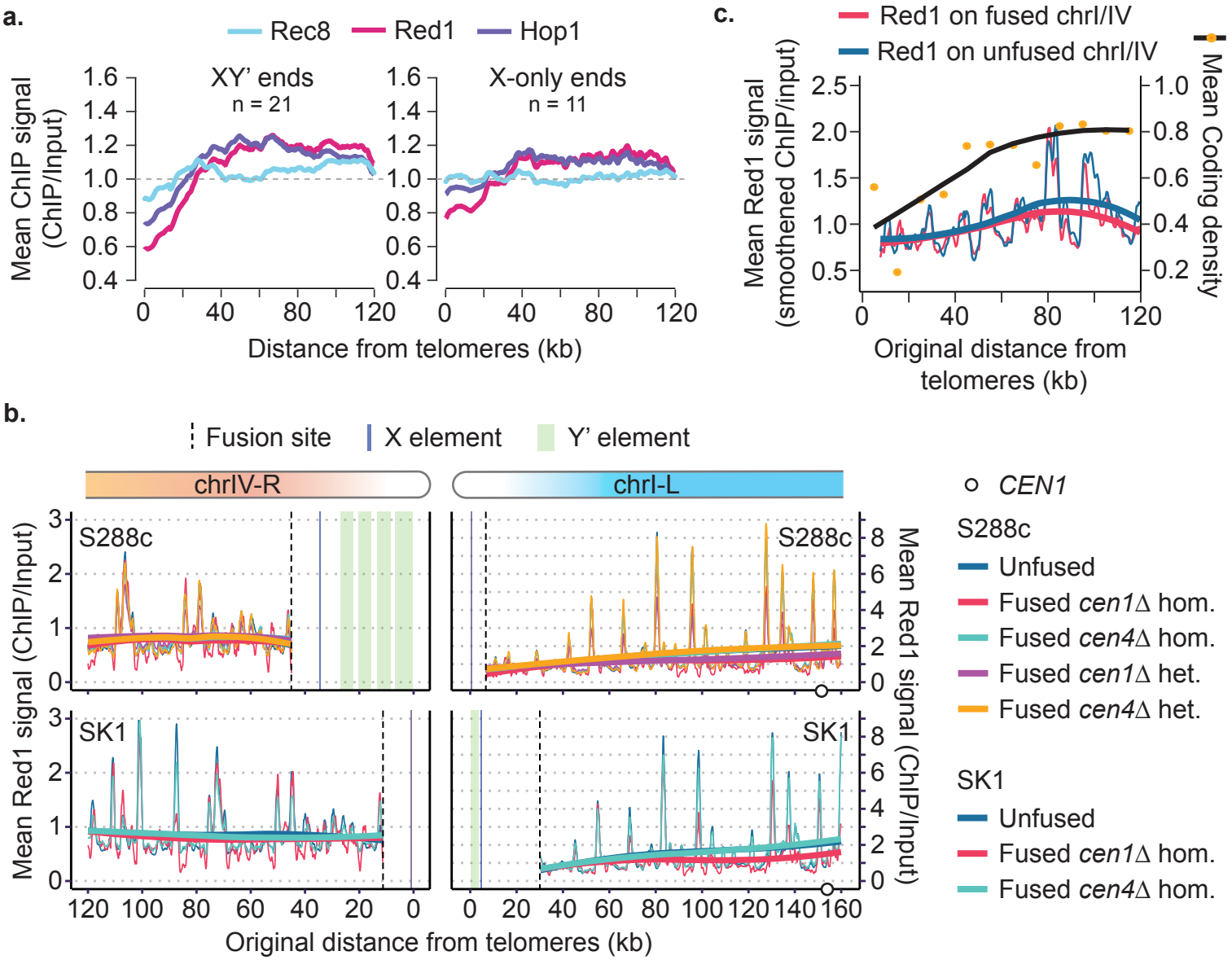

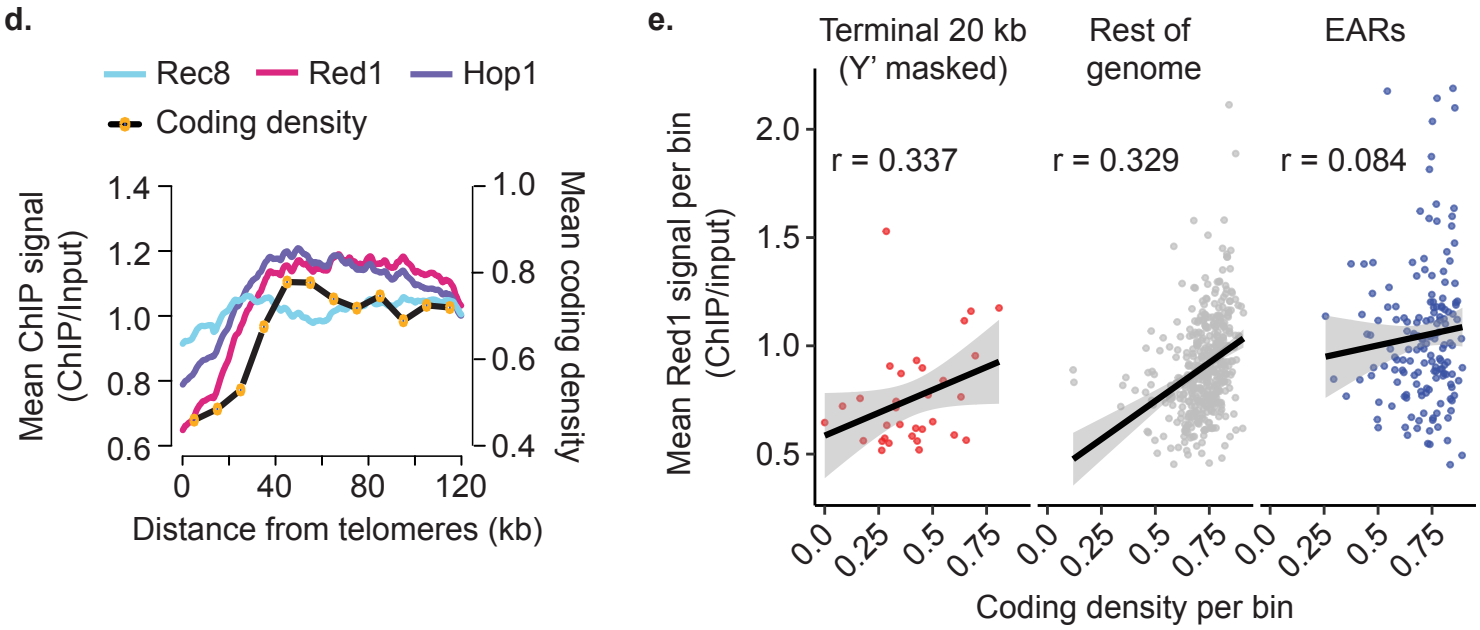

Raghavan *et al*, Fig. 2

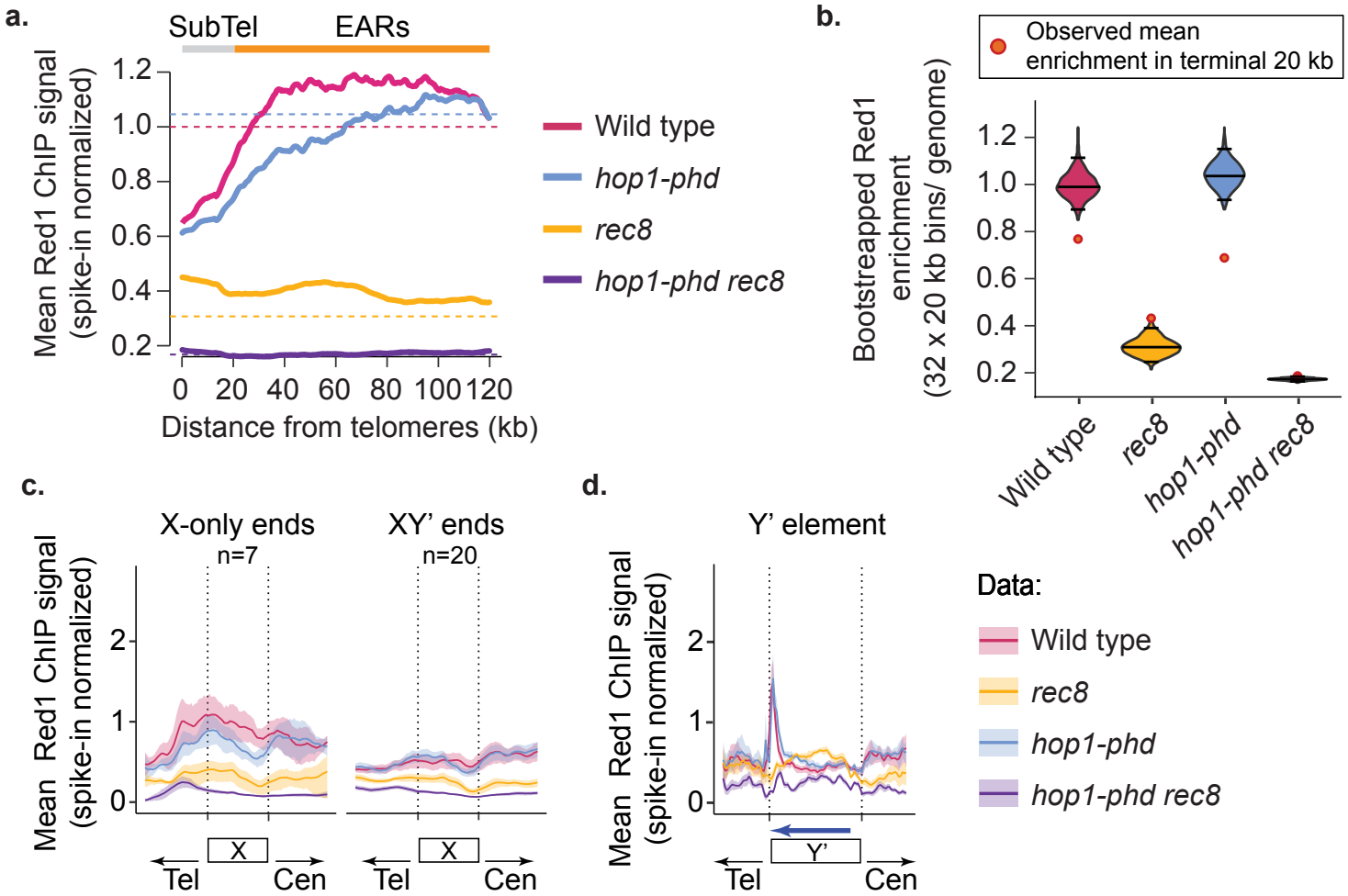
a.
SubTel
EARs
Mean Red1 ChIP signal (spike-in normalized)
1.2
1.0
0.8
0.6
0.4
0.2
0
20
40
60
80
100
120
Distance from telomeres (kb)
Wild type
hop1-phd
rec8
hop1-phd rec8
b.
Observed mean enrichment in terminal 20 kb
Bootstrapped Red1 enrichment (32 x 20 kb bins/ genome)
Wild type
rec8
hop1-phd
hop1-phd rec8
c.
X-only ends
n=7
XY' ends
n=20
Mean Red1 ChIP signal (spike-in normalized)
X
Tel
Cen
d.
Y' element
Y'
Data:
Wild type
rec8
hop1-phd
hop1-phd rec8

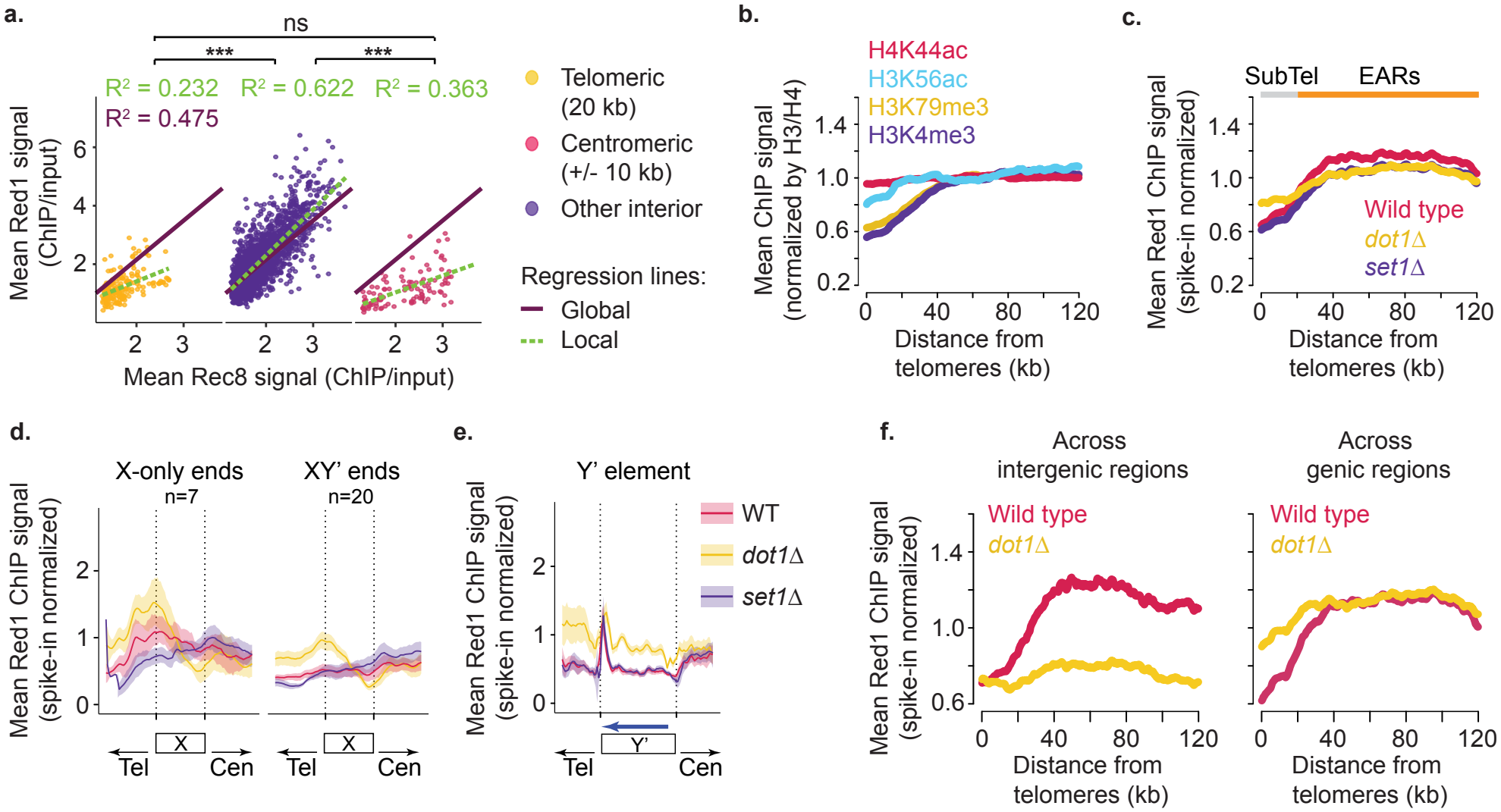

Raghavan *et al*, Fig. 4

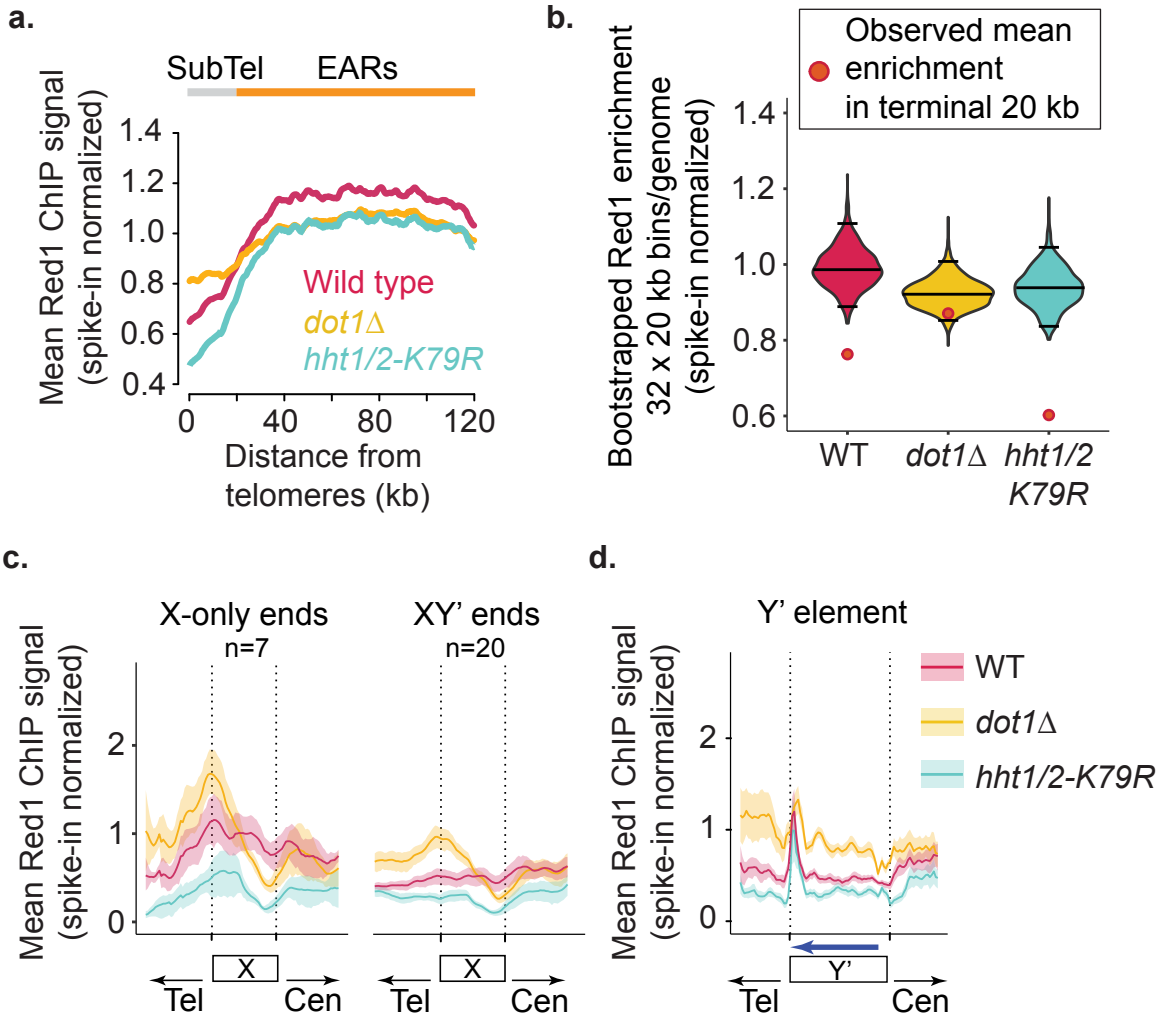

Raghavan *et al*, Fig. 5

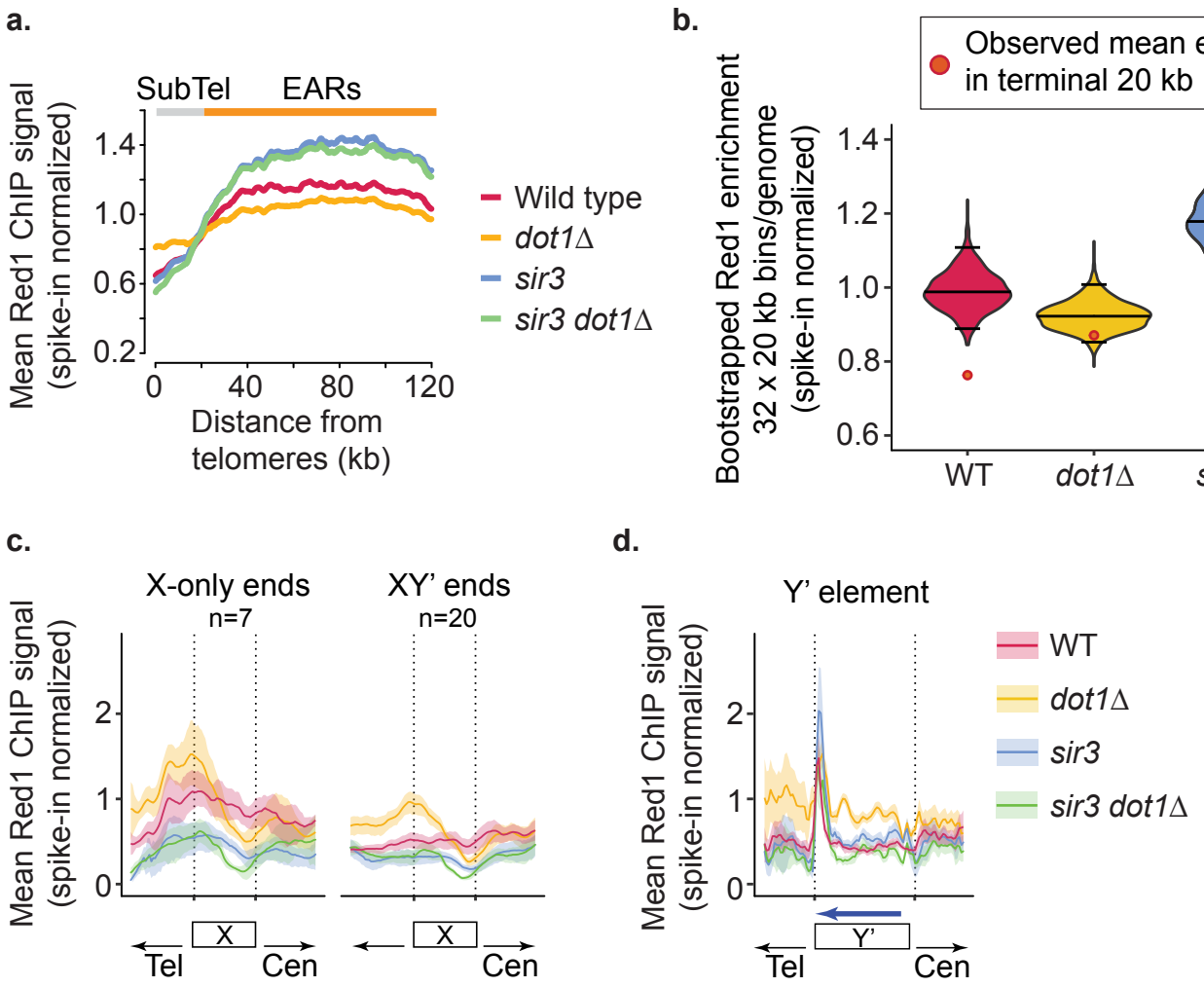

Raghavan *et al*, Figure 6

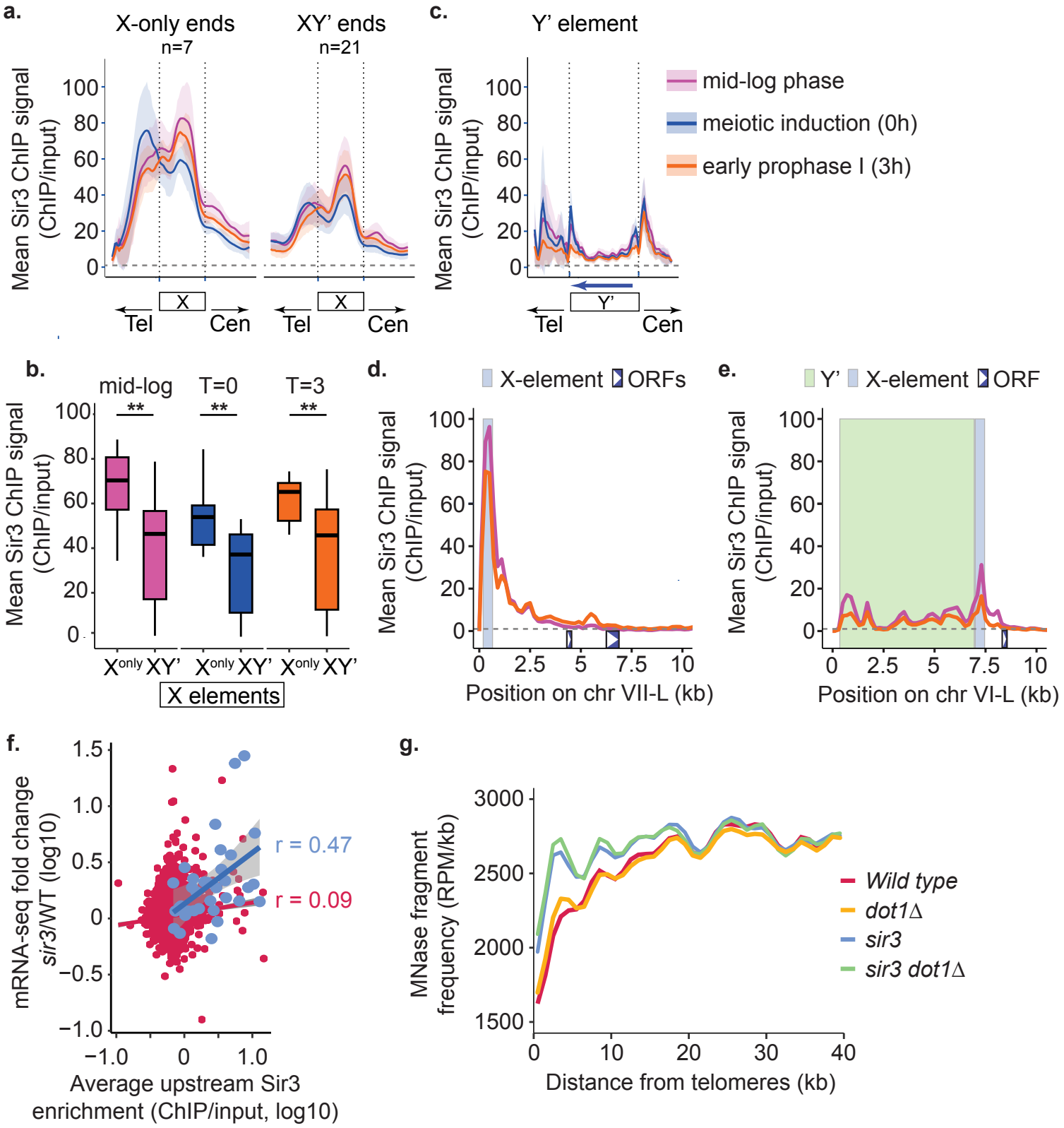

Raghavan *et al*, Fig. 7

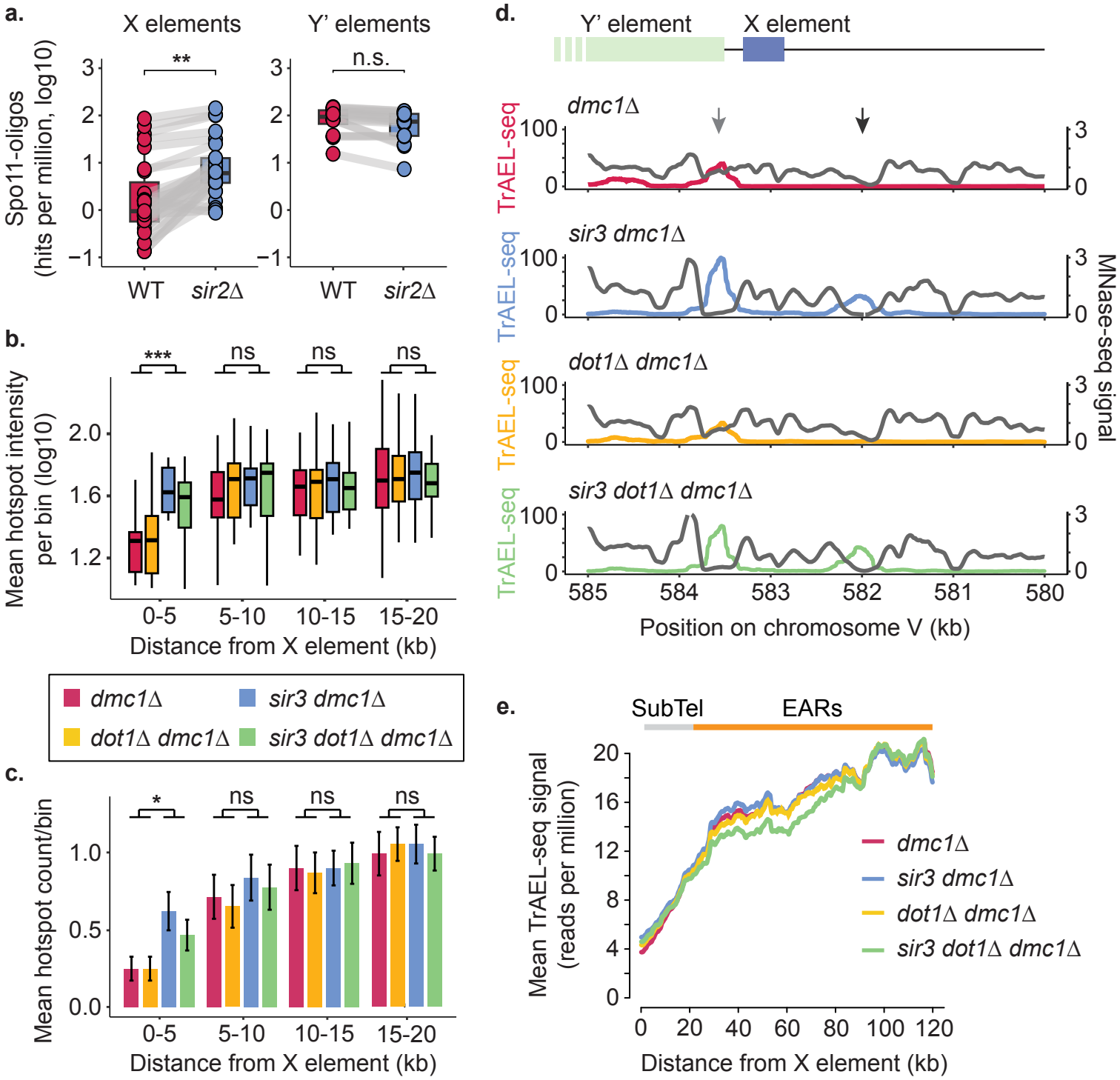

Raghavan *et al*, Fig. 8